RSC Advances

REVIEW

View Article Online
View Journal | View Issue

Cite this: *RSC Adv.*, 2026, **16**, 883

High-performance gas diffusion electrodes for next-generation CO_2 conversion technologies

D. Yureka Imali, E. Chavin J. Perera, M. N. Kaumal *
and Dhammike P. Dissanayake

Received 5th September 2025
Accepted 12th December 2025

DOI: 10.1039/d5ra06681f

rsc.li/rsc-advances

The development of CO_2 utilization technologies has seen rapid progress during the past few years. In this area of research, electrochemical CO_2 reduction (eCO_2R) has been identified as one of the promising pathways. However, this process is yet to reach industrially relevant rates of product formation. In the eCO_2R, the gas diffusion electrode (GDE) is the key component, with its architecture playing an important role. This review presents the latest advancements and opportunities in GDE structural design and materials selection, with a deep dive into the structure–performance relationship and its complex interplay in eCO_2R. Many recent research efforts have focused on improving catalysts, gas diffusion structures (gas diffusion layers (GDLs) and porous hollow fiber walls), electrolytes, and interfaces in order to optimize key performance metrics such as activity, selectivity, and stability, which are often intertwined and can complicate design efforts. The basic configuration has transitioned from conventional planar GDEs to self-supported hollow fiber GDEs (HFGDEs), along with emerging advanced forms of planar GDE, such as mesh, woven, carbon-free, and heteroarchitectural designs. These advancements have led to enhanced triple-phase boundary formation and improved mass transfer, resulting in high-performance GDEs capable of achieving ampere-level current densities (~3 A cm^{-2}), high faradaic efficiencies (FE) for target products, and extended operational stability (>100 h). Further, we discuss current bottlenecks and provide perspectives aimed at offering new insights and guiding research directions to advance the development of industrially applicable GDE-based eCO_2R systems and facilitate their practical implementation.

1. Introduction

CO_2 is a non-toxic, widely available, and sustainable carbon resource.[1–3] The electrochemical reduction of CO_2 into value-added multi-carbon products[4–7] (*e.g.*, chemicals,[8] fuels,[8,9] and energy storage molecules[8]) through clean and economical processes has gained significant interest due to its potential in high-density renewable energy storage.[4–7] The electricity used to drive the electrochemical reduction of CO_2 is sustainably generated, from sources like photovoltaics, wind turbines, hydroelectric, geothermal power stations, *etc.*[10,11] Large-scale use of CO_2 as a chemical feedstock to produce products such as urea, salicylic acid, organic carbonates, methanol, and polycarbonates would be highly advantageous as they are used in industry as well as agriculture.[5,12] The global rise in CO_2 emissions has led to significant concerns regarding climate change and environmental pollution.[13] Given environmental considerations and the global shift toward sustainable energy, electrochemical CO_2 valorisation offers a sophisticated, long-term solution to close the carbon cycle with economic advantages.[14]

Besides electrochemical methods, various biological, thermochemical, and photochemical approaches are being extensively studied for CO_2 conversion.[15] Most reactions involving CO_2 require stoichiometric amounts of organometallic reagents, excess additives or solvents, harsh reaction conditions, and complex procedures due to the inevitable formation of byproducts. Consequently, these factors lead to reduced economic benefits.[5] Further, only a small fraction of the total CO_2 abundance is utilized in the chemical industry. This is primarily due to the difficulty in achieving selective catalysis with high turnover numbers and cost-effective carbon-neutral processes due to CO_2's thermodynamic stability and kinetic inertness.[5]

The electrochemical conversion of CO_2 presents several advantages, including mild reaction conditions, enabling control over reaction rates and product selectivity through the applied potential, and offering extensive scalability due to the modular electrolyzer designs.[15] There are conventional electrochemical methods for CO_2 reduction, such as aqueous-fed electrochemical cells.[16] However, the inherently low solubility of CO_2 and the slow diffusion of gases in aqueous media result in a mass-transport-limited current density of approximately

---

Department of Chemistry, University of Colombo, Colombo 03, Sri Lanka. E-mail: mnkaumal@sci.cmb.ac.lk

30 mA cm^{-2}, which hinders industrial-scale implementation.[17] Further, several products generated by this process are also commercially produced from fossil fuels at a lower cost.[16] Moreover, the electrochemical reduction of CO_2 to C_{2+} products typically exhibits poor selectivity and demands a high overpotential.[18,19] Therefore, research on electrochemical CO_2 reduction (eCO_2R) has primarily concentrated on advancing catalysts that are both active and selective. Progress has been made in converting CO_2 into various products, such as carbon monoxide (CO), methane (CH_4), formic acid (HCOOH), ethanol (C_2H_5OH), and ethylene (C_2H_4), with relatively high selectivity but at low current densities.[16] This underscores the imperative to engineer systems capable of achieving high-performance CO_2 reduction to ensure economic viability.[16] Therefore, over the past years, significant attention has been devoted to eCO_2R, by developing advanced electrocatalysts and novel electrolyzer designs.[20]

Using gas-fed electrolyzers with gas diffusion electrodes (GDEs) has become a promising strategy to enhance the eCO_2R for commercial applications.[4,21] GDEs facilitate mass transport by ensuring sufficient CO_2 supply and strengthening the triple-phase reaction among the gaseous phase, electrocatalyst, and electrolyte.[22] GDE-based systems can potentially achieve industry-relevant current densities by overcoming the low solubility of CO_2 in aqueous electrolytes (approximately 35 mM) and shortening the diffusion path for the reaction.[16,23,24] The diffusion path from the CO_2 gas phase to the catalyst surface under GDE conditions is approximately 50 nm, whereas under non-GDE conditions, the diffusion distance from the bulk electrolyte to the electrode surface is around 50 μm.[25] Moreover, another essential aspect of advancing CO_2 reduction technology is the design and fabrication of efficient electrodes capable of ensuring long-term operational stability.[26] Therefore, in recent years, the GDE has been the focal point of intensive research as the crucial component in eCO_2R.

To carry out eCO_2R at commercially relevant product formation rates in an electrolyzer, the main requirement is to simultaneously manage the transport of electrons, water, CO_2, and protons at the cathode. GDEs play a key role in managing these vital processes.[27] Inside GDEs, there is a complex interplay among reactant and product transport, solution-phase reactions, and charge transfer kinetics.[28] These factors depend on the overall structure and composition of the GDE.[16] Therefore, identifying opportunities and challenges in multi-scale modelling to rationalize these phenomena and the design and development of GDEs accordingly, specifically tailored for enhanced eCO_2R performance, is crucial.[27]

For commercialization, it is essential to achieve both high faradaic efficiency (FE) (often greater than 95% selectivity)[29,30] and a reasonable current density (−200 to −500 mA cm^{-2}),[30] indicating high conversion. However, existing electro-reduction systems generally satisfy only one of these requirements.[29] Further catalyst activity of 100 A g^{-1},[30] stability greater than 20 000 h,[31] energy efficiency up to 75%,[28] low cell voltages (<3 V), and large cells (2.7 m^2) are required.[31] Therefore, the available strategies have yet to demonstrate satisfactory technological feasibility, economic viability, and practical applicability.

In this review, the primary focus is the GDE architecture and its rational design targeting enhanced eCO_2R performance. With a deep dive into the structure–performance relationship, here, we present a systematic evaluation of earlier technologies to the latest advancements, which is necessary to identify the progress and most critical science behind the designing phase, providing an insightful guide to developing GDEs with high activity, selectivity, stability, and scale-up prospects. Particular emphasis is placed on the significant advancements in transitioning GDE configuration from typical planar structures to hollow fiber gas diffusion electrodes (HFGDEs), directing progress toward industrially relevant performance and facilitating practical implementation. Further, we discuss the properties of GDEs affecting eCO_2R, the rational design of GDE components leading to efficient electrochemical conversion of CO_2 to C_{2+} products, existing challenges, and future possibilities. Specific examples from the literature published since 2020 are discussed with advanced technologies. Fig. 1 illustrates the overview of the core content presented in this review. Ultimately, we aspire to motivate efforts to make future research in eCO_2R using GDEs more appealing from an industrial point of view.

2. Electrochemical reduction of CO_2

2.1 Reaction fundamentals

CO_2 is a linear and centrosymmetric molecule with zero dipole moment. Its carbon center is electrophilic.[15] CO_2 is a highly stable form of carbon, characterized by a C═O bond energy of 805 kJ mol^{-1}. The direct decomposition of CO_2 into CO and O_2 involves a significant enthalpy change of 283.0 kJ mol^{-1} under standard conditions (1 atm, 298.15 K).[15] The reduction of CO_2 involves multiple pathways, each consisting of several steps, which can result in different products. The tailored catalytic activity and selectivity determine the specific target product.[32] The first step in initiating the eCO_2R process is the activation of CO_2 molecules. It has a very negative redox potential of up to −1.9 V *versus* the reversible hydrogen electrode (RHE). The reduction of CO_2 by coupling it with an electron to form adsorbed $CO_2^{\bullet-}$ is particularly difficult.[32,33]

There are four redox reaction pathways for the activation of CO_2. Pathways I and II are known as concerted proton–electron transfer reactions. Pathways III and IV involve charged or strongly polarizable intermediates, where selectivity depends on pH and cation effects.[32]

Path I:

$$* + CO_2 + H^+ + e^- \rightarrow *COOH$$

Path II:

$$* + CO_2 + H^+ + e^- \rightarrow *OCHO$$

Path III:

$$* + CO_2 + H^+ + e^- \rightarrow *CO_2^-$$

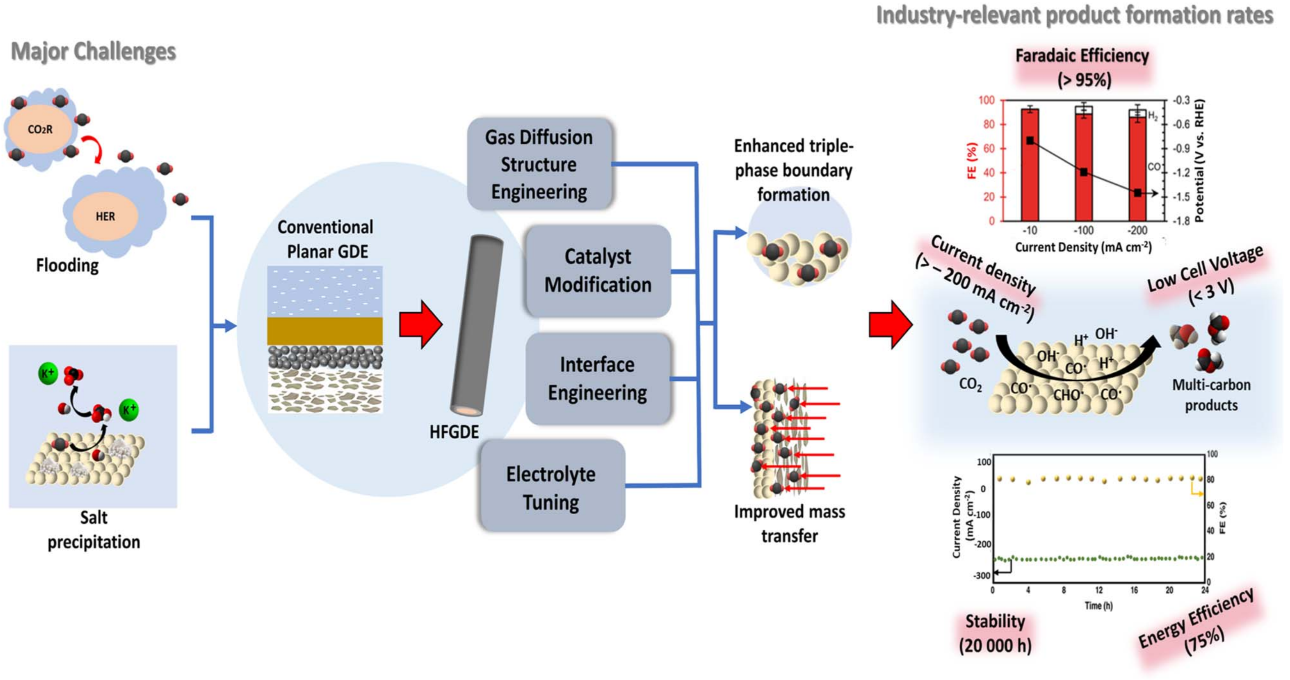

Fig. 1 Schematic illustration summarizing the scope of this review.

Path IV:

$$* + H^+ + 2e^- \rightarrow *H^-$$

Here, * denotes the active sites on the catalyst surface, and *COOH, *OCHO, $*CO_2^-$, and $*H^-$ represent the adsorbed moieties on the catalyst surface. The reduction pathways of CO_2 are intricate, owing to the involvement of different possible intermediates, resulting in multiple products. Therefore, both catalyst and energy are essential for the eCO_2R process to produce desired products with reduced overpotential.[32] Following the activation of a CO_2 molecule by an applied overpotential, the subsequent reactions involve multiple single-step processes that include both protons and electrons. These reactions are closely followed to overcome the slow kinetics typically associated with CO_2 reduction. Together, these individual steps form what is known as CO_2 reduction pathways.[34] Depending on the number of carbon atoms in the resulting molecules, products from CO_2 reduction can include C_1 (single carbon), C_2 and C_{2+} (two carbons), C_3 and C_{3+} (three carbons) products. These products are formed through processes involving concerted proton–electron transfers or electrons at various potentials. Therefore, different reaction pathways or conditions can lead to different carbon-containing products during CO_2 reduction.[32]

2.2 Performance parameters

The performance of an eCO_2R system is assessed through multiple metrics that impact the capital and operational expenses of the entire process. There are several key metrics, including FE, current density, energy efficiency, overpotential and stability. FE is the percentage of charge used to produce a specific product relative to the total charge consumed,[16] indicating the selectivity towards a particular eCO_2R product.[15,16,35] High FE reduces the need for extensive downstream product separation and lowers the total current required to achieve a desired production rate.[16]

The reaction rate is another key performance indicator of a CO_2R system, and its determination often depends on the type of catalyst used.[15] For example, in molecular electrocatalysis, a well-defined structure of active sites allows the turnover frequency to be a reliable indicator of reaction rates. However, when using bulk or nanostructured materials as electrocatalysts, the presence of active sites with unknown structures is common. In these cases, current density serves as an indicator of the eCO_2R rate. Considering practical convenience, the reaction rate is often represented by the geometric current density, which is the catalytic current normalized by the geometric surface area of the electrode.[15] The high current density reduces the capital costs. However, operating at high current densities decreases the energy efficiency of the system due to significant ohmic losses and undermines the stability of the eCO_2R process.

Energy efficiency refers to the percentage of energy stored in desired products relative to the total input energy, which correlates with the overall cell voltage. High energy efficiency is crucial for minimizing the electricity costs involved. Stability is a crucial factor in assessing the efficiency of eCO_2R, as it affects maintenance and replacement costs, as well as electrolyzer downtime. The cathode and membrane are the two main components that limit the stability of the eCO_2R system.[16] Another critical performance metric is the overpotential, defined as the absolute difference between the applied potential where a substantial amount of the target product is generated and the equilibrium potential of the corresponding eCO_2R half-reaction.[15]

3. Different types of systems for eCO_2R

3.1 Non-gas-fed electrochemical cells

This approach employs an electrochemical cell featuring a liquid–solid double-phase contact system (Fig. 2a).[36] The eCO_2R system consists of a cathode, an anode, a CO_2-containing electrolyte, and a membrane. The cathode functions as the electrocatalyst for the CO_2 reduction reaction, while the anode facilitates oxidation reactions like oxygen evolution. The electrolyte is essential for transporting charged species and facilitating CO_2 transport to the electrocatalyst surface and it critically affects the energetics of CO_2 reduction. Meanwhile, the membrane segregates the oxidation and reduction products, ensuring charge equilibrium.[24] The conversion of gaseous CO_2 into valuable chemicals encompasses several chemical and physical processes, which can be divided into four distinct steps: solvation dynamics, activation, preferential dimerization, and higher-order selectivity.[24] CO_2 from the gas phase first dissolves in the solution, forming aqueous CO_2. This aqueous CO_2 then reacts with water to form carbonic acid (H_2CO_3). However, in a CO_2-saturated aqueous solution at pH 6.8, the predominant species is bicarbonate (HCO_3^-).[24,37] Aqueous electrolytes reach saturation at 34 mM CO_2 under ambient conditions, restricting the rate of CO_2 transport to the electrocatalyst. Overcoming this mass transport limitation is essential to achieve industrially viable CO_2 reduction rates.[24] The low solubility of CO_2 results in low current densities,[38–40] which are typically limited to of <60 mA cm^{-2}.[41–43] This falls significantly short of the potential industrial standards, which require current densities in the range of hundreds of mA cm^{-2}.[38–40] At higher current densities, hydrogen evolution often supersedes other reactions due to the rapid kinetics of water reduction and constraints in CO_2 mass transfer.[44–47]

Further, the infusion of CO_2 into the electrolyte restricts the use of highly alkaline pH values.[23,48] Therefore, the CO_2 and proton concentrations, and consequently the pH, fluctuate during catalysis, highlighting the need for a more advanced model for designing electrocatalytic interfaces.[49,50] At the electrocatalytic surface, CO_2 undergoes activation, which involves its adsorption in a conformation suitable for further reactivity. The two predominant activation geometries are *OCHO and *COOH.[51,52] After adsorption, a series of proton and electron transfers take place, leading to reduction reactions.[51]

3.2 Gas-fed electrolyser systems

Gas-fed CO_2 electrolysers offer a prominent solution to the solubility challenge by introducing CO_2 into the cell in its gaseous state.[43,53] As depicted in Fig. 2b, a three-phase contact system for eCO_2R is used, allowing intimate contact between gaseous CO_2, the electrolyte, and the electrocatalyst.[54–57] This method can be effectively implemented using GDEs.[43,53] CO_2 in the gas phase, with a diffusion coefficient of about 0.1 $cm^2\ s^{-1}$, diffuses nearly four orders of magnitude faster than in the liquid phase,[58] thus presenting a more efficient CO_2 transfer for electrochemical CO_2 reduction reaction (eCO_2RR).[36] These three-phase contact systems provide numerous benefits for eCO_2RR, including the ability to use high pH electrolytes, which are not easily applicable in double-phase contact systems, to enhance eCO_2RR electron transfer kinetics.[59,60] This approach enables efficient CO_2 electrolysis to valuable commodity chemicals at high current densities.[61] At present, two major types of gas-fed CO_2 electrolyzers have been successfully integrated the GDEs:[62] electrolyzers with a membrane electrode assembly (MEA) where the cathode GDE is in direct contact with a membrane[63,64] and electrolyzers with a flowing catholyte where the GDE is in direct contact with an electrolyte.[62,65,66] Compared to planar electrodes, GDEs are complex systems that require the adjustment of various design parameters to optimize the eCO_2RR at the three-phase interface of catalyst, electrolyte, and gaseous CO_2.[38]

4. Gas diffusion electrodes

In gas-phase eCO_2R, the GDE is the key component that facilitates the conversion of CO_2 into desired chemicals and fuels.[16] GDEs are porous electrodes that feature a catalyst layer in direct contact with the electrolyte (Fig. 3a).[53] Their applications can be

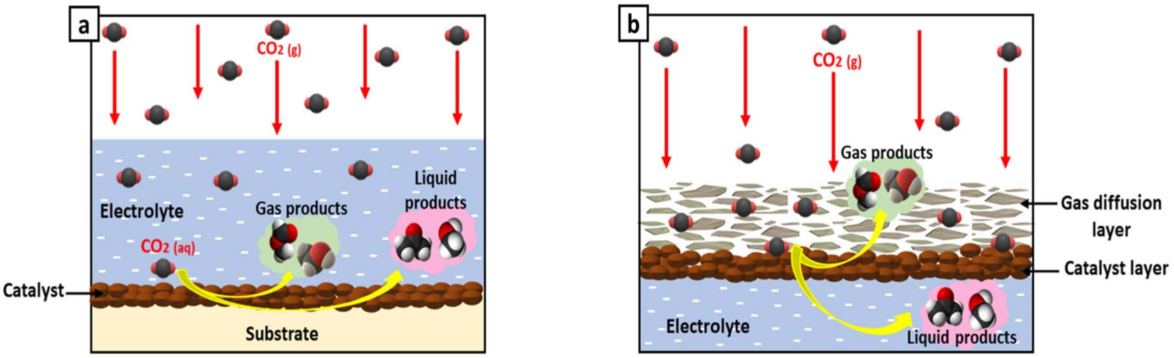

Fig. 2 Schematic representation of operational principles and CO_2 flow in (a) aqueous-fed and (b) gas-fed CO_2 electrolyzer systems.

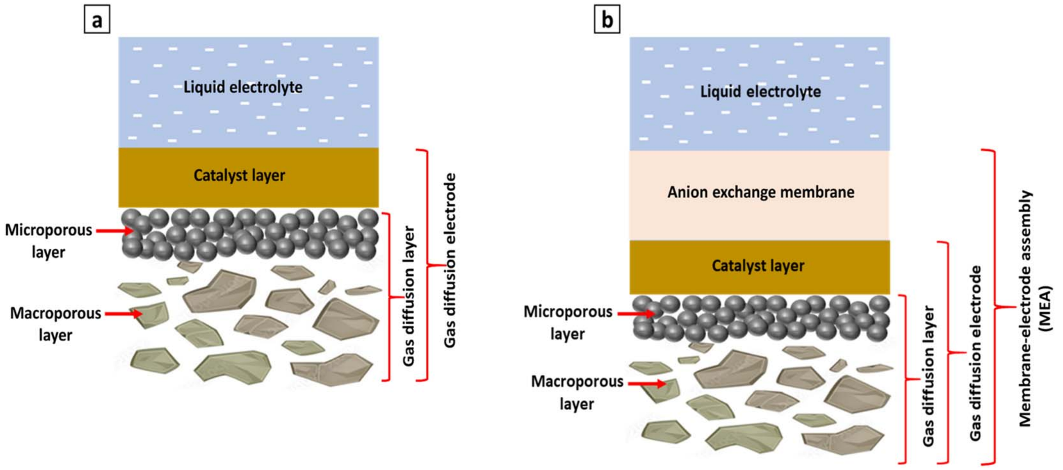

Fig. 3 Schematic representation of (a) typical planar GDE and (b) zero-gap GDE.

found in electrochemical energy conversion devices such as fuel cells.[67,68] In GDEs, the path length of CO_2 diffusion to the catalyst surface is significantly reduced, as compared to typical planar electrodes used in H-cells.[21] Therefore, the GDE ensures a concentrated CO_2 environment near the catalyst surface during high current density operations, which is typically a challenging target to achieve even in an alkaline aqueous system.[48] The GDE allows the manipulation of reaction conditions, such as employing alkaline electrolytes, to enhance activity and selectivity, capabilities that would otherwise be unattainable.[16]

4.1 Structure and principle of planar GDEs

A GDE comprises a catalyst layer deposited on a gas diffusion layer (GDL).[16,43,69,70] The GDL is a hydrophobic, conductive[16] and porous structure positioned between the catalyst layer and the gas flow channel or field.[71] The porous matrix of the GDL permits the transport of gases while restricting the movement of liquids.[72] Apart from delivering reactants, the GDL performs several other crucial functions including, releasing gaseous reaction products, providing mechanical support and electrical contact for the catalyst, and regulating the amount of electrolyte in the catalyst layer.[73,74] Typically, the GDL consists of two layers: a macroporous substrate and a microporous layer.[71] It fulfills two main roles: facilitating gas transport to the catalyst layer and offering structural support to the catalyst. The GDL is designed to be hydrophobic, preventing pore blockage by the electrolyte and ensuring efficient gas transport to the catalyst layer.[43] Various GDLs have been examined, including structures based on carbon,[75] metal, polytetrafluoroethylene (PTFE), and membranes and carbon-based GDLs are the most commonly reported, often featuring hydrophobic properties introduced by PTFE coating within the carbon matrix.[76]

There are two types of GDLs: the single-layer, which consists solely of a macroporous layer or substrate, and the dual-layer, which combines a macroporous layer with a microporous layer. Among these types, dual-layer GDLs are often employed, especially in CO_2 electrolysers, to mitigate electrolyte flooding of the GDE.[43] The macroporous substrate offers mechanical stability and electrical connectivity for the GDE while distributing CO_2 gas through its large pores. This substrate is typically constructed from conductive carbon fibers or titanium foam.[16] The microporous layer, situated above the macroporous substrate and often made of carbon and hydrophobic agents to manage catholyte flooding[43] and enhance the interfacial electrical connection.[16] Its hydrophobic characteristics and nanoscale pores permit the passage of gas molecules while preventing liquid water from penetrating.[16] The morphology, porosity, thickness, and hydrophobicity of the microporous layer are vital for eCO_2R due to the intricate gas and liquid transport processes involved. These properties can be optimized by altering its composition.[77,78] The gas flow field, which is directly in contact with the macroporous layer, serves the dual roles of gas diffusion and current collection.[43]

Catalysts are usually applied as nanoparticles with a typical loading of 1 mg cm^{-2}. This enables the specific catalyst activities of 200 A g^{-1}.[30] The catalyst layer is created by applying a suspension of PTFE like hydrophobic agents and catalyst particles onto the microporous layer.[79] Considerable attention has been devoted to designing electrocatalysts to enhance the efficiency of CO_2 reduction.[80–82] The performance of the catalyst layer is determined by the morphology and composition of the active catalyst particles as well as its overall structure. In GDEs, the three primary catalyst layer structures are two-dimensional (2D) thin films, three-dimensional (3D) nanostructures, and three-dimensional (3D) nanoparticulate layers. In addition to achieving high FE for desired products and operating at high current densities, ensuring stable long-term performance is essential for the practical application of a catalyst in eCO_2RR.[14,83] In gas-phase eCO_2R, high operating current densities induce substantial changes in the catalyst layer, including variations in pH and CO_2 concentration.[16]

Various types of materials serve as catalysts, including metals, metal-free compounds, molecular catalysts, enzymes, and microbes.[43] With metal-based electrocatalysts being the most widely utilized type for eCO_2R, the application of an external bias initiates a complex, multi-proton–electron-coupled transfer process yielding a diverse range of value-added products. Noble metals (*e.g.*, Au, Ag, and Pd) have been reported as highly efficient electrocatalysts, with their structures and morphologies significantly impacting both FE and current density. However, limited availability and relatively high cost hinder their large-scale application.[84] Non-noble metals, such as Zn[84] and Cu, have also gained significant attention. The choice of catalyst determines the primary target intermediates (*e.g.*, Ag for CO, Cu for C_2H_4, Sn for HCOOH, *etc.*).[62]

Copper (Cu) has been the focus of intensive research as a catalyst for eCO_2RR due to its unique ability to produce multicarbon products, which is linked to its moderate CO* binding energy.[4,85,86] Cu is recognized as the sole metal capable of catalyzing the eCO_2RR to hydrocarbons efficiently,[85,87,88] albeit with issues of poor selectivity.[85] Further, the high overpotentials and inadequate partial current densities of Cu-based materials during C_{2+} production lead to significant efficiency losses.[89] The challenge of stabilizing Cu^+ under eCO_2RR conditions persists.[4] Including modifier elements has been proposed as an effective strategy to mitigate the reduction tendency of Cu^+ at negative potentials.[90,91] Zn is also widely employed in eCO_2R owing to its low-cost, well-defined structure, high surface-to-volume ratio, and excellent selectivity toward CO. Further, Zn-based electrocatalysts are capable of efficiently handling large volumes of CO_2 within the appropriate local electrochemical environment.[84]

A major challenge in eCO_2R research is the absence of a standardized experimental setup and methodology for quickly evaluating the performance of various catalytic materials that show potential for eCO_2R technology development.[29] Zero-gap GDEs attract much attention as they demonstrate promising characteristics for scaling up to commercial levels.[92] As depicted in Fig. 3b, in a zero-gap GDE configuration, the cathode is in direct contact with the membrane that separates it from the electrolyte solution (the anolyte) containing the anode.[93] These zero-gap GDEs interfaced to ion exchange membranes, form membrane-electrode assemblies,[94] and offer several advantages over typical GDEs that expose the catalyst layer directly to the electrolyte. These advantages include reduced ohmic losses,[95] enhanced catalyst stability, and the prevention of issues caused by the formation of gaseous products directly at the electrode/electrolyte interfaces.[96] This membrane serves two primary functions. It regulates the amount of water acting as a reactant in the eCO_2R, preventing kinetic limitations due to water scarcity.[27] Additionally, it ensures that gaseous products formed by eCO_2R in the catalyst layer do not enter the anode compartment.[93]

4.2 Hollow fiber gas diffusion electrodes (HFGDEs)

HFGDE is a novel electrode configuration that emerged as an alternative to planar GDEs.[97,98] It is a novel self-supported GDE that serves as a working electrode and a gas diffuser.[99] Their unique tubular architecture, abundance catalytic active sites, and facile fabrication have shown great potential in enhancing eCO_2RR performance.[97] Fig. 4 depicts the schematic illustration of the typical HFGDE and its cross-sectional view. HFGDEs are easy to produce using the industrially viable dry-wet process[100,101] and offer tunable fiber and pore structures.[100] In contrast to conventional flow-by GDEs,[102] the tubular shape and porous hierarchical walls facilitate a forced gas flow-through the three-phase reaction interface.[99] This configuration facilitates eCO_2RR on the outer surface of the HFGDE, while the resulting products and unreacted CO_2 reside on the electrolyte side. This reduces the concentration gradient, improving CO_2 delivery to the catalyst layer.[102] The penetration of the CO_2 gas through the porous hollow fiber wall to the catalyst/electrolyte interfaces happens due to the CO_2 gas pressure developed in the lumen side of the hollow fiber. Compared to the conventional planar GDEs, which typically comprise a superhydrophobic macroporous layer, a microporous layer, and a catalyst layer, HFGDEs present a simplified assembly process,[101,102] eliminating the need for a separate gas chamber and flow cell for gas diffusion.[102,103] Therefore, transitioning from traditional planar GDEs to HFGDEs has significantly enhanced the eCO_2RR kinetics[103] and enable the reaching of industrially viable current densities exceeding 200 mA cm^{-2},[103] ultimately demonstrating significant promise in gas-phase electrolysis.[22]

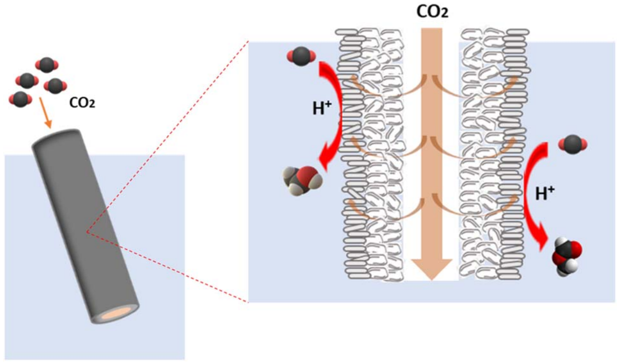

Fig. 4 Schematic representation of a typical HFGDE and its cross-sectional view.

5. Recent progress in the rational design of GDEs

5.1 Advancements in planar GDEs

The advancements in planar GDEs can be broadly classified into two main categories: structural modifications and microenvironmental tuning. Structural modifications primarily aim to optimize the GDE architecture by tailoring the catalyst layer and engineering the GDL. Microenvironment tuning involves manipulating the local chemical environment around the catalyst surface to favor desired reaction pathways.[104] This is typically achieved through electrolyte modification and interface engineering. The following sections discuss these advancements in detail, which have driven progress toward high-performance planar GDEs.

5.1.1 Structural modifications. GDEs demonstrate favorable prospects for advancing the scale-up and commercialization of CO_2 electrolysis processes.[43] Owing to improved CO_2

mass transport and minimized diffusion lengths within the catalyst layer, GDEs are capable of achieving higher current densities compared to traditional electrodes.[53] However, the durability of gas-fed electrolysers is limited, resulting in a significant decline in performance after a few operational hours.[105] In industrial settings, achieving both high selectivity and stability under high current densities is rarely observed. This issue primarily arises during the industrial-scale implementation of research findings.[4] In order to overcome these limitations, the use of catalysts has emerged as a major area of research, attracting significant attention from scientists. In recent years, numerous studies have reported on catalysts designed to enhance the performance of the eCO_2RR, particularly with the increasing interest in producing multi-carbon products.[106]

At present, Cu has been recognized as the most prominent metal catalyst for facilitating C–C bond formation. However, intensive research is still required to overcome the remaining low selectivity of its untreated form for C_{2+} products. Therefore, significant efforts have been directed toward developing modified Cu catalysts by altering the oxidation state, morphology, and exposed facets and creating bimetallic alloys containing Cu.[106] Recent advances with Cu bimetallic materials have shown improved selectivity in eCO_2RR compared to Cu alone, suggesting that the secondary metal may play a crucial role in modifying adsorption energies.[85] Song *et al.* reported a boron-doped Cu (B-Cu) (Fig. 5a) catalyst that facilitates efficient eCO_2R at current densities relevant to industrial applications, employing a GDE electrolysis system.[4] The catalyst's remarkable performance is mainly ascribed to the stabilization of Cu^+ species facilitated by the introduction of B.[13] Due to its Lewis acidity, B tends to accept electrons from Cu. This interaction tunes the local electronic structure of Cu, creating positive valence sites and enhancing its Lewis acidity. These effects are advantageous for promoting the formation of C_{2+} products in eCO_2R.[13]

A novel approach used to improve the catalytic activity is the polymer modification of the Cu surface or integration of polymer into a Cu-based catalyst layer.[106,107] Modifying the Cu surface with polymers containing oxygen, nitrogen, or fluorine

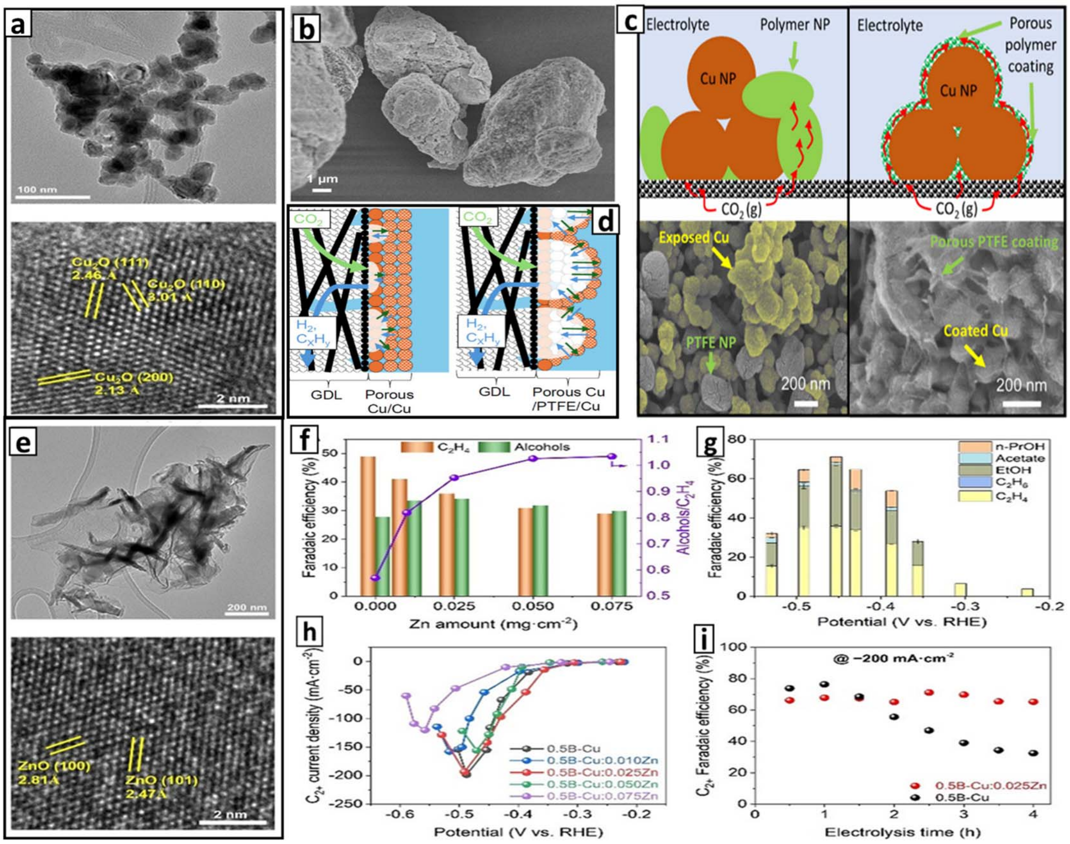

Fig. 5 (a) TEM image (upper) and HRTEM image (lower) of B-Cu nanoparticles. Reproduced with permission.[4] Copyright 2021, Wiley-VCH Verlag GmbH & Co. KGaA, Weinheim. (b) SEM image of micro-granules. (c) Schematic illustrations (upper) and SEM images (lower) of the catalyst layer consisting of a simple mixture of Cu and PTFE nanoparticles (left) and PTFE nanofilm-coated Cu catalyst (right). Reproduced with permission.[106] Copyright 2023, Royal Society of Chemistry. (d) Gas transportation on porous Cu/Cu/GDL (left), and porous Cu/PTFE/Cu/GDL (right). Reproduced with permission.[110] Copyright 2025, Wiley-VCH Verlag GmbH & Co. KGaA, Weinheim. (e) TEM image (upper) and HRTEM image (lower) of Zn nanosheets. GDE performances; (f) FE for producing different C_{2+} products with varying amounts of Zn, (g) FE for the formation of various C_{2+} products using 0.5 B-Cu:0.025 Zn catalyst at different potentials, (h) partial current density for the formation of C_{2+} products at different potentials on B-Cu electrodes with varying amounts of Zn and (i) FE for the formation of C_{2+} products in the presence and absence of Zn and stability over time. Reproduced with permission.[4] Copyright 2021, Wiley-VCH Verlag GmbH & Co. KGaA, Weinheim.

containing functional groups has several advantages on eCO_2RR. These include increased hydrophobicity of the cathode, suppressing competing HER, and increased C_{2+} product selectivity through stabilizing the reaction intermediates.[108,109] Various research groups have conducted theoretical studies on understanding the effect of the polymer modification of Cu on C_{2+} product selectivity and have identified that functional groups such as –COOH and $–CF_2$ influence the binding energies of key intermediates of eCO_2RR.[106] Pellessier *et al.* developed PTFE-modified Cu nanoparticles as a catalyst layer for eCO_2RR, forming an interconnected porous 3D micro-granule structure (Fig. 5b). The FE for C_{2+} products of 78% at a high current density of 500 mA cm^{-2} has been achieved due to the nearly complete surface coverage of the Cu nanoparticles by the porous PTFE film and the presence of a large Cu–polymer interfacial area (Fig. 5c).[106] In another study, Seki *et al.* developed a porous Cu–PTFE hybrid electrocatalyst. They reported decreased FE for H_2 (11.6%) and high FE for C_2H_4 (51.1%) under the current density of −300 mA cm^{-2} for over 24 h. This enhanced performance can be attributed to the addition of PTFE, which mitigates water penetration into the catalyst layer, thereby providing a secure pathway for CO_2 supply to the reaction sites and facilitating the removal of gas-phase products (Fig. 5d).[110]

In a study conducted by Zheng *et al.*, they utilized heteroatom (N, P, S, O) engineering on Cu catalysts to achieve ampere-level current density for CO_2 to C_{2+} electrolysis, which is critical for industrial applications. At high current densities, insufficient CO intermediate (*CO) coverage on the catalyst surface promotes the competing HER, thereby hindering the eCO_2RR. By suppressing HER, heteroatom engineering enhances *CO adsorption on the Cu surface, significantly reducing the energy barrier for C–C coupling. Among these heteroatoms, N-engineered Cu catalysts exhibited the best performances for C_{2+} product formation with FE of 73.7% under −1100 mA cm^{-2} and an energy efficiency of 37.2% under −900 mA cm^{-2}.[111]

Another key issue is that cathodic corrosion at high cathodic potentials restricts the long-term stability of Cu-based catalysts. To mitigate this problem, less noble metals like Zn can be used as sacrificial anodes to protect the catalyst. This strategy has been effectively utilized by Song *et al.* incorporating Zn nanosheets (Fig. 5e) into the B-Cu catalyst to improve its stability during eCO_2R. This approach significantly enhanced the long-term stability of C_{2+} product formation. Further, this modification ensured the stability of active Cu^+ species even at high reduction potentials and caused the formation of *OCO to occur at a less negative potential, contributing to the excellent electrochemical conversion of CO_2 to C_{2+} products (Fig. 5i). The optimal Zn amount for minimizing cathodic Cu corrosion while preserving adequate activity for C_{2+} product formation has been reported to be 0.025 mg cm^{-2}. The 0.5 B-Cu:0.025 Zn composition gives the maximum current density for C_{2+} product formation that is attained across almost the entire potential range, with a measured value of −194 mA cm^{-2} at −0.49 V *vs.* RHE (Fig. 5h) and the highest faradaic efficiency for C_2 product formation at −0.45 V *vs.* RHE and a total current density of −200 mA cm^{-2} (Fig. 5f and g).[4]

While there have been significant efforts in optimizing catalytic activity, attention to design and function of the GDEs has been relatively low. Importantly, catalyst properties are not the sole factor influencing selectivity. This has been effectively demonstrated by the work of Gu *et al.* They examined several other factors influencing selectivity. Further, they showed that the selection of an appropriate membrane in zero-gap GDEs is critical to achieving high selectivity and current efficiency for different target products. In this regard, four different polymer electrolyte membranes, Fumasep FAA-3-PK-75 (PK75), Nafion 115 (N115), Fumasep FAA-3-50 (FAA50), and Sustainion X37-50 Grade 60 (G60) have been studied. The anion exchange

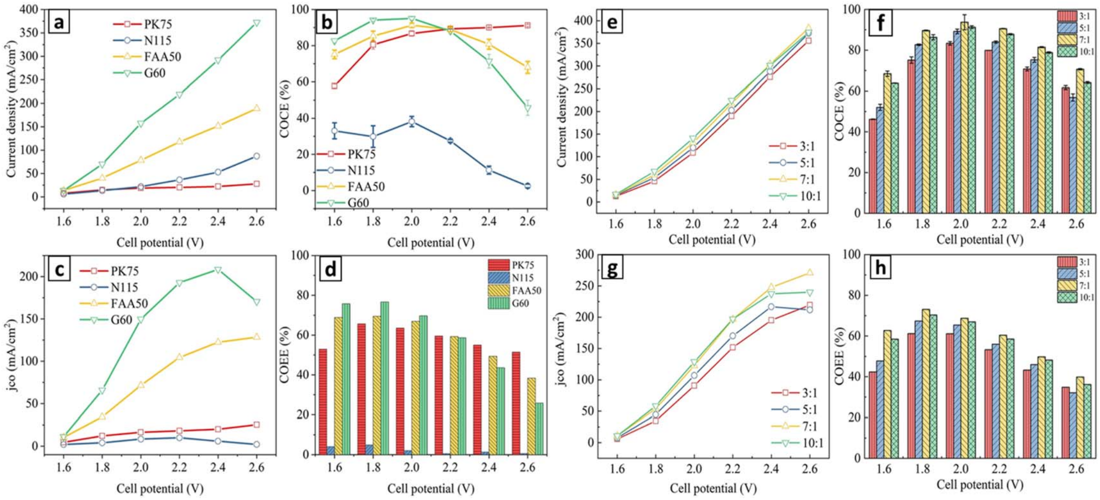

Fig. 6 Cell performance with different membranes as a function of cell potential. (a) Total current density (j_{total}), (b) current density for CO production (COCE), (c) partial current density of CO production (j_{CO}), and (d) energy efficiency for CO production (COEE). Cell performance with different PTFE contents as a function of cell potential. (e) j_{total}, (f) COCE, (g) j_{CO} and (h) COEE. Reproduced with permission.[112] Copyright 2021, Springer.

membranes improved the function of GDE by increasing the current efficiency. Particularly, the G60 membrane displayed improved performance in the conversion of CO_2 to CO (Fig. 6a–d). The high-performance of G60 membrane is characterized by its thinness (50 μm) and its exceptionally low average area resistance (0.045 Ω cm^{-2}) under alkaline conditions.[112] Cation exchange membranes such as N115 exhibit greater selectivity for hydrogen and formate products. As a consequence of this, the hydrogen evolution reaction (HER) was more prone to occur. Moreover, in the study conducted by Alinejad *et al.*, it was revealed that employing anion exchange membranes results in high current densities with the same catalyst, compared to the use of cation exchange membranes such as Nafion. However, Nafion was found to be more effective as a binder in the catalyst layer for enhancing performance.[92]

In eCO_2R, maintaining a low overpotential is critical for energy efficiency and reaction control. Lower overpotentials tend to favour specific reaction pathways, which can help in selectively producing the desired product. However, higher overpotentials might drive multiple competing reactions, leading to a mixture of products and thus low selectivity. It has been reported that optimization of the mass ratio of total catalyst to binder agent (*e.g.*, PTFE) leads to achieving high current density, current efficiency, and energy efficiency at low cell potential. Gu *et al.* reported a total current density of 131.0 mA cm^{-2} at a low cell potential of 2.0 V, with a current efficiency of 93.72% and an energy efficiency of 68.7% for CO production, using a total catalyst-to-PTFE mass ratio of 7 : 1 (Fig. 6e–h). Further, PTFE proved to be more suitable than Nafion as a binder for GDE preparation for eCO_2R.[112]

In zero-gas GDEs, effective control of membrane hydration is essential for maintaining optimal performance. Insufficient hydration can result in higher cell resistance and significant energy losses, while excessive hydration can lead to GDL flooding, compromising the transport of gaseous reactants to the catalyst.[70] In the study conducted by Gu *et al.*, findings revealed that introducing a thin liquid buffer layer between the cathode and the membrane can enhance catalytic performance by promoting the efficient diffusion of CO_2 gas to the catalyst surface. By introducing a thin liquid pH buffer layer, a triple-phase boundary is created. This setup allows CO_2 molecules in the gas phase to diffuse rapidly to the catalyst's surface, faster than they would in the liquid phase. This improved diffusion enhances the selectivity of the catalyst for eCO_2R while partially suppressing the competing HER. However, adding a liquid buffer layer leads to a notable increase in the overall resistance between the two electrodes (Fig. 7a). This increase in resistance caused a decrease in current density. Consequently, this high resistance also implies greater energy consumption in industrial applications, making the process less efficient. For optimal application, the buffer layer must be exceedingly thin.[112] It can be suggested that the liquid buffer layer maintains an optimal gas–liquid interface *via* enhancing ionic conductivity, maintaining catalyst hydration, and mitigating local pH variations. This is a cathode feeding method. The cell performance has been further evaluated using other different cathode feeding techniques, including a humidified-CO_2 feeding method and a CO_2-saturated $KHCO_3$ feeding method. These various methods influenced the CO_2 concentration available to the catalyst surface. In the CO_2-saturated $KHCO_3$ feeding method, the current density for CO production gradually decreases beyond a certain point due to the low solubility of CO_2 in the aqueous solution, promoting HER. The mass transfer of CO_2 molecules under this method was the lowest. The humidified-CO_2 feeding method yielded the best performance (Fig. 7b).[112]

Applying carbon support to catalyst nanoparticles is an effective strategy to enhance both the activity and selectivity. In the study conducted by Alinejad *et al.*, the observed deterioration in selectivity was attributed to the degradation of the catalyst layer.[92] The supported Au nanoparticles achieve significantly high current densities compared to their unsupported counterparts. Supporting Au nanoparticles on carbon greatly improves the accessibility of the particles for chemical reactions. This can be attributed to the large specific surface area, high porosity, and excellent electron conductivity of carbon that acts as the catalyst support. Moreover, this modification increased the activity of the catalyst layer while reducing the propensity for the HER. The supported Au catalyst layers tend to be more hydrophobic compared to unsupported catalyst layers. Depositing the catalyst as a metal layer makes the surface more hydrophilic, which is typical for metal surfaces (Fig. 7c).[92]

Moreover, the ionomer-to-catalyst ratio has demonstrated a significant impact on the selectivity (Fig. 7d). High concentrations of Nafion ionomer lead to a less active catalyst layer, where the HER becomes more prominent. The absence of an ionomer or the use of a low-anion ionomer results in high current densities, which reduces capital costs, making it highly advantageous for industrial applications. However, the absence of an ionomer results in high cell resistance, highlighting the inadequate ionic conductivity of the catalyst film. Further, there is a risk of agglomeration of nanoparticles during electrolysis.[92] The degree of particle agglomeration is associated with the type and amount of ionomer in the catalyst layer. This can be ascribed to ionomer-dependent particle growth, which can be influenced by variations in local pH.[92]

Flooding presents a significant issue that arises within these systems. It is a complex phenomenon involving various physicochemical processes that affect GDLs.[93] It can occur in GDEs that are in direct contact with liquid electrolytes[113] or enclosed by ion exchange membranes (zero-gap GDEs).[114,115] Flooding in electroreduction systems can be attributed to several phenomena. These include the wettability of GDEs,[116,117] electrowetting from potential-induced changes in electrolyte-solid surface tension[118–120] humidity of reactant gases,[121] presence of reaction intermediates[120] and products[122] (*e.g.*, liquid water formed as the reaction product), electrolyte pH,[120] temperature differentials across the cell[120] and pressure differentials between gas and liquid at the interface,[123,124] salt precipitation due to ion accumulation,[120,125] water pumping driven by ion concentration gradients between the reaction interface and bulk electrolyte,[125,126] water vapor condensation,[54] the thickness of the membranes used[127] and eCO_2R liquid products decrease the electrolyte–electrode surface tension leading to reduced capillary pressure.[122]

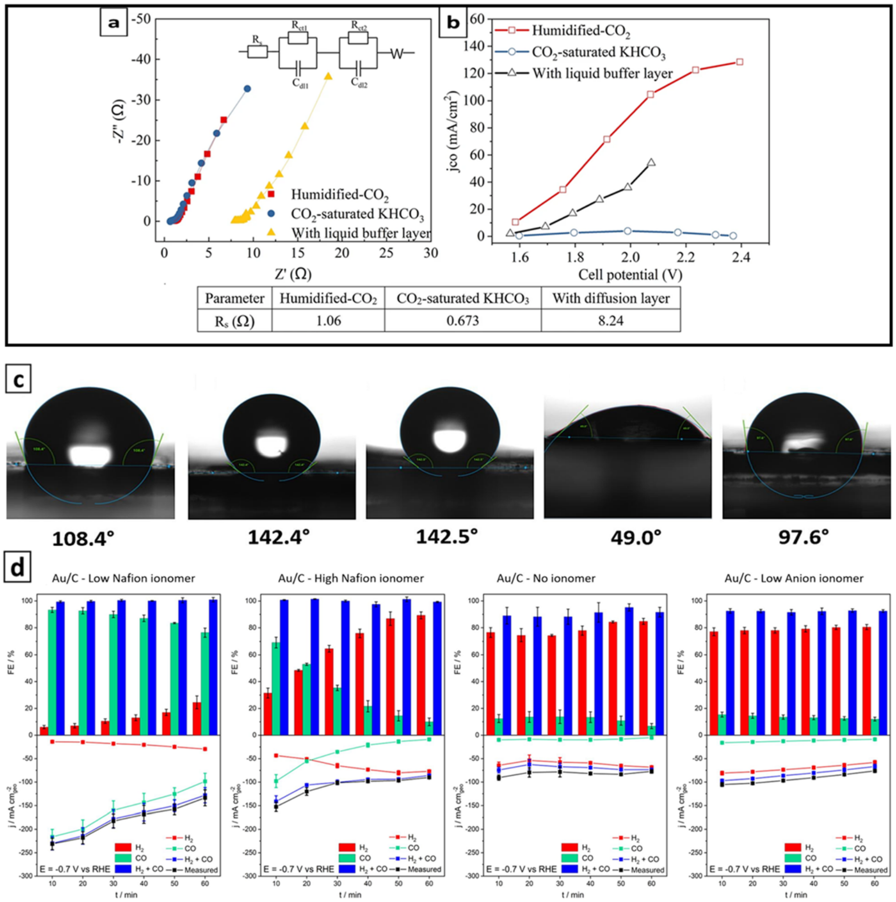

Parameter	Humidified-CO$_2$	CO$_2$-saturated KHCO$_3$	With diffusion layer
R$_s$ (Ω)	1.06	0.673	8.24

Fig. 7 (a) EIS results for different cathode feeding methods under open-circuit conditions. (b) j_{CO} as a function of the cell potential. Reproduced with permission.[112] Copyright 2021, Springer. (c) The surface contact angle of unsupported Au NPs with low Nafion ionomer, supported Au/C catalyst with low Nafion ionomer, supported Au/C catalyst with high Nafion ionomer, supported Au/C catalyst with no ionomer, and supported Au/C catalyst with low anion ionomer from left to right. (d) FE and current densities of the gaseous products obtained from eCO$_2$RR on supported Au/C catalyst with changing the ionomer. Reproduced with permission.[92] Copyright 2024, Elsevier.

In eCO$_2$R electrolyzers, flooding often coincides with the presence of precipitated salts inside or on the surface of GDEs.[128] Hence, the presence of observed precipitates serves as an indicator of flooding. These salts are either components of the electrolyte solution or are produced when a component reacts with CO$_2$. Flooding and salt precipitation can obstruct or entirely block the transport of CO$_2$ to the catalyst. Consequently, a shift from eCO$_2$R to H$_2$O reduction occurs, causing a significant decrease in the overall FE of eCO$_2$R.[93] This issue is most commonly observed in eCO$_2$R electrolyzers that use alkaline electrolytes where flooding and precipitating exist as mutually perpetuating processes. Alkaline electrolytes react with the CO$_2$, forming precipitates like potassium carbonate or bicarbonate, decreasing the hydrophobicity of the GDE[129] and one of the main causes of performance degradation.[92] These carbonate deposits on the surface of the GDEs obstruct the gas transmission channels, thereby limiting CO$_2$ diffusion and mass transfer.[130] As a result, electrolyte permeates into the microporous layer, leading to the formation of additional precipitates.[129] Further movement of liquid electrolytes throughout the entire GDE, known as electrolyte perspiration, may occur.[131] For catalytic performance and stability, both the total electrolyte content and its spatial distribution within a GDE are critical factors.[93] Interestingly, it has been found that cracks in the microporous layer enhance the reaction by improving the mass transport of gaseous CO$_2$ to the catalyst and by facilitating the removal of excess electrolytes from the catalyst layer. Electrolyte perspiration through cracks in the microporous layer can help prevent or delay the complete flooding of the micropores.[93]

Concerning electrolyte ion intrusion, Kong *et al.* conducted a study to investigate electrolyte transport through microporous layers, aiming to prevent electrode flooding and salt precipitation in commercial eCO$_2$R reactors. They examined flooding and perspiration phenomena using zero-gap GDEs with systematically varied microarchitectures, featuring microporous layers with different crack abundances (Fig. 8a). The study was conducted with alkaline anolyte and at different stages of electrolysis. Their results demonstrated that submillimeter cracks in the microporous layer of GDEs used for CO$_2$ electrolysis are crucial for electrolyte management. These cracks provide a direct pathway for electrolyte drainage, effectively preventing or at least delaying the flooding of the catalyst

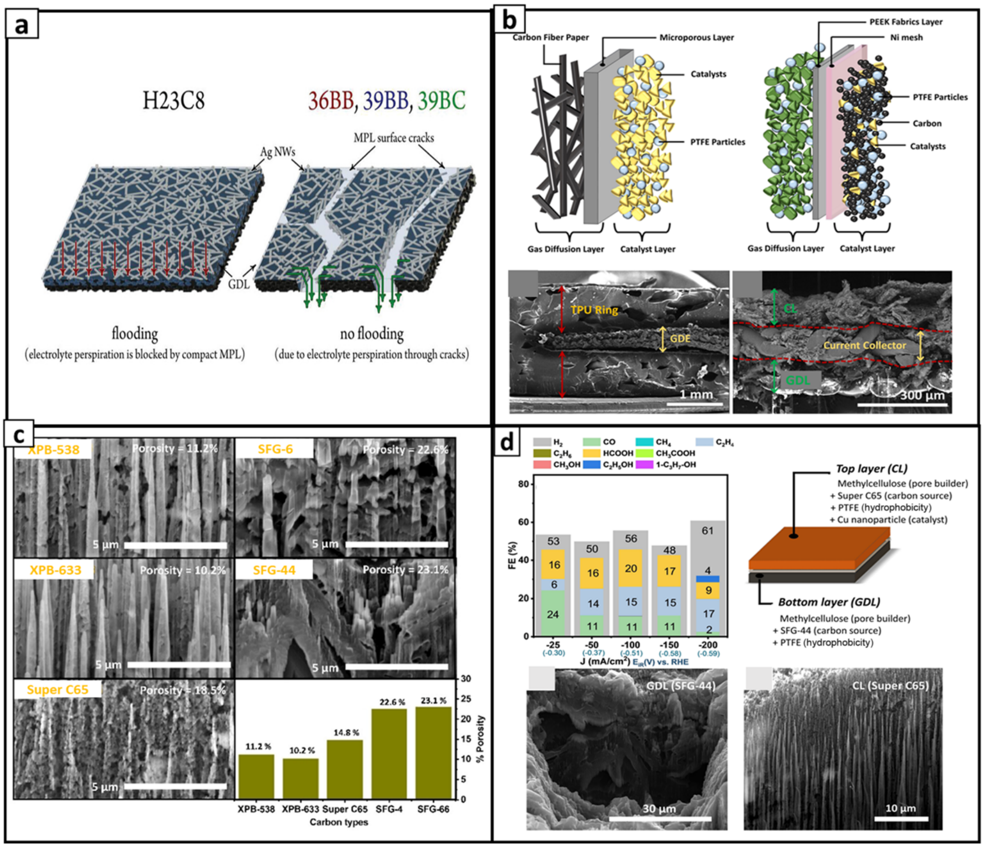

Fig. 8 (a) Schematic illustration of the electrode flooding and electrolyte perspiration phenomena of the catalyst layer supported with non-cracked (left) and cracked (right) microporous layer. Reproduced with permission.[93] Copyright 2022, Wiley-VCH Verlag GmbH & Co. KGaA, Weinheim. (b) Schematic representation of the structural difference between a typical GDE (upper left) and the novel GDE design (upper right); SEM micrographs of the cross-section of novel GDE with low magnification (below left) and high magnification (below right). (c) The porosity of GDEs prepared with different carbon materials. (d) FE of novel hybrid GDE (upper left), schematic representation of hybrid GDE configuration (upper right), SEM image of the GDL with high porosity using SFG-44 (lower left), and SEM image of the catalyst layer with less porosity using Super C65 (lower right). Reproduced with permission.[38] Copyright 2022, Chemistry Europe.

layer.[93] However, electrolyte perspiration through cracks can lead to considerable unintended losses of CO_2 due to its neutralization. Therefore, to optimize the efficiency of CO_2 usage in electrolyzers, it is crucial to identify conditions that minimize both electrode flooding and perspiration-related reactant losses.[92] Further, Alinejad *et al.* demonstrated that adequate porosity in the catalyst layers can effectively reduce precipitate formation under low current densities, and utilizing materials like carbon as a catalyst support significantly enhances porosity. Its high specific surface area, high porosity, and excellent electron conductivity make carbon an excellent catalyst support.[92]

Maintaining high current densities is necessary for large-scale industrial applications.[17] Although some highly effective electrocatalysts can selectively produce desired reaction products, these reactions typically occur at relatively low current densities, usually in the range of several mA cm^{-2} to tens of mA cm^{-2}. However, these current densities are significantly lower than what is required for commercial applications, where much higher values are needed for practical and efficient large-scale operations.[132] For instance, achieving current densities greater than -300 mA cm^{-2} is essential for the formation of C_2H_4. Even though some groups have reported current densities exceeding -1.5 A cm^{-2}, the long-term stability of electrode configurations operating under these conditions is challenging.[17] In a typical GDE setup, two common challenges arise during measurements. These are the electrolyte flooding into the catalyst layer at high current densities, leading to the loss of the three-phase boundary[36,76] and the catalyst layer peeling off as the reaction advances, resulting in the parasitic HER due to the increased exposure of the carbon surface.[38] To address these challenges, novel fabrication techniques for GDEs must be developed by adjusting structural parameters and allowing for flexible arrangement of the GDL, catalyst layer, and supporting electrodes. This approach helps stabilize the GDE structure and enhance its hydrophobic characteristics.[38]

In the fabrication process, it is crucial to consider the interaction of various factors, systematically control multiple structural parameters and establish a balanced configuration accordingly. For instance, the thickness of GDEs must be tailored effectively to enhance gas delivery and electron transport rates, and to regulate the electrolyte film to balance CO_2

transport resistance to the catalyst and ensure optimal ionic conductivity within the catalyst layer. Moreover, porosity and hydrophobicity are crucial parameters. These properties can be adjusted by altering the hydrophobic additives and pore builder content.[38] For instance, PTFE can be used to decrease the average pore diameter. Further, PTFE increases the contact angle, increasing the hydrophobicity of internal pore walls.[30,133,134] However, since these additives are insulating compounds, they affect the electrical conductivity of the GDEs, necessitating the inclusion of conductive materials like carbon black to mitigate this issue.[38]

In this context, Wang *et al.* proposed a scalable and transferable approach for the fabrication of a carbon-based asymmetrical hybrid GDE. Their research focused on fine-tuning the parameters that impact the performance of carbon-based GDEs. The proposed novel GDE configuration comprised five main components from bottom to top: a GDL, a polyetheretherketone (PEEK) fabric layer, a nickel mesh, a catalyst layer, and a dispersed PTFE layer (Fig. 8b). The eCO_2R was notably improved by controlling the porosity and hydrophobicity. The HER was simultaneously suppressed. Additionally, the GDE was encased with two thermoplastic polyurethane rings to prevent side gaseous leakage. Furthermore, the overall thickness of the GDE was optimized to approximately 340 μm, with the catalyst layer and GDL each measuring about 120 μm.[38]

They demonstrated the impact of layers, porosity distribution and strategies for optimizing critical parameters to achieve the final structure of the GDEs with improved performance and a lower overpotential.[38] When designing GDEs, it is crucial to consider the number of layers and their thickness. Thin GDEs with a low number of layers (such as two) are unable to sustain high current densities. This limitation arises from electrowetting and flooding, which are induced by the potential-driven decrease in capillary pressure between the electrolyte and the GDL substrate.[135] GDEs with a high number of layers, such as five, are prone to cracking during hot-pressing and heating procedures. This cracking causes undesirable electrolyte leakage under measurement conditions. Further, the increased number of layers reduces CO_2 permeability and subsequently lowers eCO_2R activity. Optimal performance is achieved with four-layer GDEs, as they demonstrate higher selectivity for CO_2 reduction products and reduced H_2 evolution.[38]

The porosity of the GDE is crucial for maintaining consistent gas transport, which is essential for creating and sustaining a three-phase boundary within the GDE. During the fabrication process, it is essential to carefully control the applied pressure and materials selection (the amount of pour builder (*e.g.*, methylcellulose) used and the type of carbon materials employed). These factors significantly influence the porosity of the GDE. Even though increasing the quantity of the pour builder such as methylcellulose has minimal impact on the porosity, the type of pour builder used has a significant impact (*e.g.*, latex as a pour builder improves the eCO_2R performance significantly). According to the findings of Wang *et al.*, GDEs fabricated with 100 bar pressure achieved the highest yields of C_1 and C_2 products and the lowest overpotentials. In contrast, GDEs fabricated with high pressures, such as 300 bar and 500 bar, showed similar eCO_2R activity but produced more hydrogen.[38]

The activity and selectivity of eCO_2R are heavily influenced by the characteristics of the carbon material used, such as particle size, shape, pore structure, and hydrophobicity. The carbon materials play a critical role as the main skeleton within the GDE structure. They facilitate electronic conductivity across the electrode and offer structural support.[136] Therefore, when selecting carbon materials, their ability to promote the selectivity for the desired C_2 product in the eCO_2R should be a key consideration. The porosity of carbon materials directly impacts cell performance, necessitating the selection of carbon materials with specific pore characteristics tailored to different purposes (Fig. 8c). A large pore size and high porosity are preferred for the bottom part (GDL) of the GDE to enhance effective CO_2 transport through its structure and provide larger areas of the three-phase boundary created by the solid catalyst, liquid electrolyte, and gaseous CO_2 inside the GDE. Conversely, a smaller pore size is recommended for the upper part (catalyst layer) of the GDE to mitigate the risk of electrolyte flooding by letting electrolyte soak. This hybrid structure of the GDE, which employs high porosity in the GDL and less porosity in the catalyst layer, enhances the eCO_2R performance. Further, the hybrid GDA configuration effectively reduces the hydrogen evolution (Fig. 8d).[38] In this hybrid configuration, a layer of PEEK fabric, which is a thermoplastic exhibiting exceptional mechanical characteristics,[137] was inserted between the nickel mesh and the GDL. This helps prevent electrolyte flooding into the GDL, enhances the selectivity for valuable C_2 products and suppresses the HER. In the study of Wang *et al.*, additionally, a PTFE layer was applied to the catalyst layer as the exposed carbon active sites tended to promote the HER.[38]

Although carbon-based GDLs are commonly used, they exhibit very poor stability in CO_2 reduction applications.[123] Flooding is the primary cause of this instability.[26,30] Within a few hours of operation, the GDL often becomes flooded, leading to reduced selectivity for CO_2 reduction reaction.[123,124] However, the immediate onset of flooding, typically within 1 h, during CO_2 electrolysis lacks a clear explanation.[76] Due to the flooding, some of the pores in the initially hydrophobic GDL become filled with liquid. This water ingress obstructs the CO_2 from reaching the catalyst's active site by extending the diffusion path and promotes salt precipitation, which can permanently block the pores. Consequently, flooding shifts the system's performance towards the HER, resulting in a critical failure of the CO_2 electrolysis system.[76]

Flooding can be mitigated by employing a more hydrophobic GDL. However, this approach compromises electrical conductivity. In addition, the excessive use of ionically conductive binders essential for adhesion among catalyst particles and between the catalyst layer and the hydrophobic substrate leads to decreased electrical conductivity by blocking the catalytic surface sites. Conversely, an inadequate amount of binder can cause nanoparticle agglomeration during GDE fabrication, leading to weak adhesion to the GDL and detachment during electrolysis, ultimately compromising the overall stability. Further, the chemical stability of the GDL substrate determines the durability of carbon-based GDEs in CO_2 electrolyzers. Chemical degradation reduces the hydrophobic nature of the pore network, allowing electrolytes to penetrate more easily through the pores at a lower pressure difference between the liquid and gas phases, thereby restricting the gas flow.[30]

Yang *et al.* investigated the electrochemical factors contributing to the premature flooding of carbon-based GDLs during CO_2 electrolysis that is independent of eCO_2R. Their findings are crucial for designing GDEs that optimize product selectivity and catalyst stability. It was found that the wetting characteristics and resistance of the GDL to premature flooding depend on the applied potential and the associated electrochemical activity of the carbon in the GDL. Reducing the catalyst onset potentials and maintaining operation within an optimal potential range can extend the lifetime of CO_2 electrolyzers before flooding occurs (Fig. 9a). Moreover, electrochemical characterization of carbon GDLs, with and without catalysts, suggests that the high overpotential required for eCO_2R initiates hydrogen evolution (Fig. 9b).[76] At open-circuit potential, the flooding resistance of GDEs is influenced by their material characteristics (*e.g.*, pore structure and wettability).[30,138] Small hydrophobic pores give high flood resistance.[30,133,134] The surface becomes more hydrophilic upon the application of an electrical potential, which is known as the electrowetting effect. This phenomenon describes the decreasing of water contact angle of the inner surfaces of pore network when the electrode becomes charged during electrolysis. This allows the electrolyte to infiltrate the pore network, hindering the gas diffusion.[30,139]

Particularly at high current densities, GDEs encounter flooding issues attributed to electrowetting, which typically results in a reduced concentration of CO_2 at the triple-phase boundary due to its low solubility. In the study conducted by Song *et al.*, to address the issue of flooding, different quantities of PTFE were incorporated into the catalyst ink to improve the hydrophobicity of the B-Cu catalyst. Increasing the PTFE content relative to the total catalyst mass resulted in enhancing the hydrophobic properties of the B-Cu GDE. The catalyst loading was adjusted to optimize the gas–liquid–catalyst interphase. This optimization resulted in achieving a maximum FE of 78% for C_{2+}, specifically 49% C_2H_4, 22% C_2H_5OH, and 7% C_3H_7OH. These results were obtained using a B-Cu GDE with 10% PTFE and a catalyst loading of 0.5 mg cm^{-2} at a current density of −200 mA cm^{-2} and a potential of −0.45 V *vs.* RHE (Fig. 9c).[4]

In addition to wetting properties and microstructure,[140] flooding behavior depends on the differential pressure in CO_2 electrolyzers with a flowing catholyte.[124] Flooding can occur when the differential pressure between the liquid and the gas phases surpasses the interfacial forces of the pore network.[62] Fluctuations in this pressure are caused by the density difference between the gas and liquid phases and can alter the local flow regime along the GDE. When this pressure difference is sufficient to push the electrolyte into the pore network, liquid breakthrough occurs. Baumgartner *et al.* studied the effect of GDE structure, differential pressure, and cathode potential on the flooding and performance of gas-fed CO_2 electrolyzers with a flowing catholyte. For that, six commercial GDL materials with different microstructures (carbon cloth and carbon paper) and thicknesses (Fig. 10a) were coated with an Ag catalyst and evaluated under differential pressures corresponding to different flow regimes (gas breakthrough, flow-by, and liquid breakthrough) (Fig. 10b).[62]

Their findings reveal that the cathode potential and GDE microstructure significantly influence differential pressure, and GDEs with a suitable structure can sustain robust CO_2 reduction even in the presence of flooding and electrolyte breakthrough,

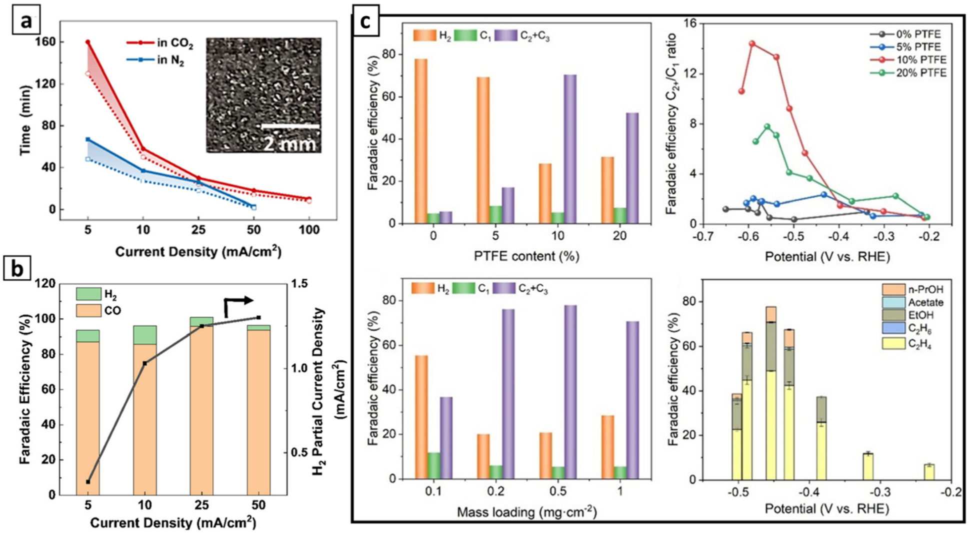

Fig. 9 (a) Times of flooding occurrence; empty circles indicate when liquid droplets first appeared, while solid circles indicate complete flooding of the GDE. The inset displays an image of a fully flooded sample. (b) FE and partial current density for H_2 on Ag/GDL during eCO_2RR at various cathodic current densities. Reproduced with permission.[76] Copyright 2021, American Chemical Society. (c) FE representation with different catalyst loadings, PTFE contents, and at different potentials. Reproduced with permission.[4] Copyright 2021, Wiley-VCH Verlag GmbH & Co. KGaA, Weinheim.

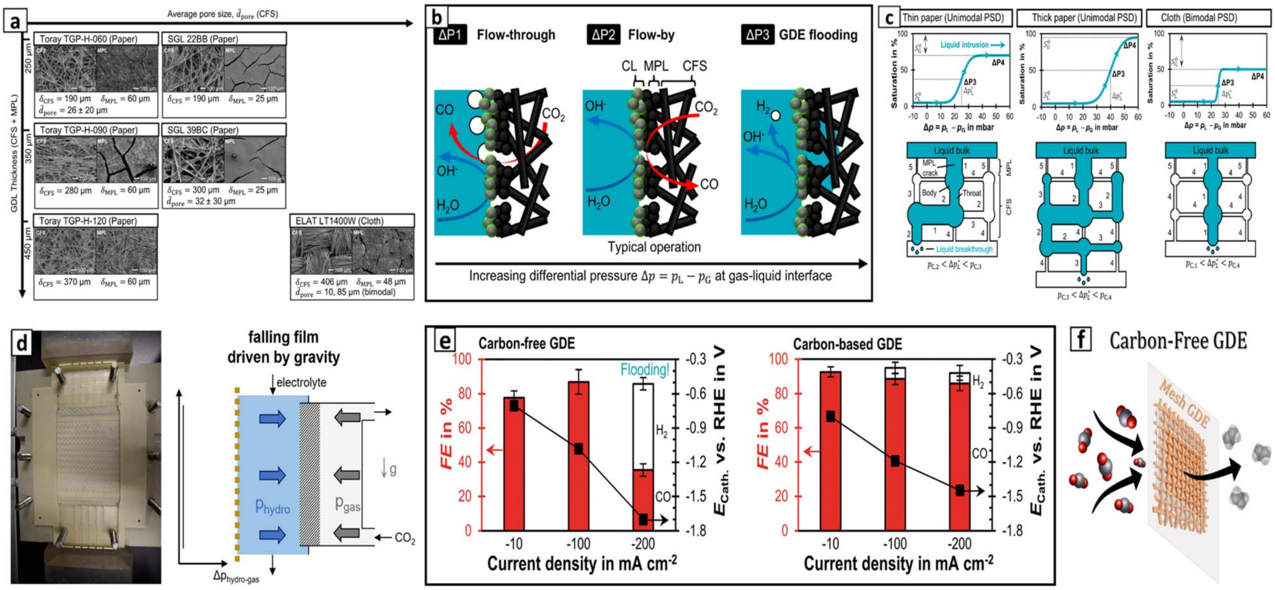

Fig. 10 (a) SEM images depicting microstructures of different commercial GDE substrates. (b) Schematic illustration of flow-through regime, flow-by regime, and GDE flooding regime, respectively, from left to right. (c) Saturation behaviour of different carbon fiber substrate structures. Reproduced with permission.[62] Copyright 2022, American Chemical Society. (d) Falling film design (left) and schematic illustration of the falling film concept (right). Reproduced with permission.[31] Copyright 2023, Elsevier. (e) FE for CO and H_2 of carbon-free GDE (left) and carbon-based GDE as a function of current density (right). Reproduced with permission.[30] Copyright 2023, Royal Society of Chemistry. (f) Carbon-free mesh GDE. Reproduced with permission.[17] Copyright 2024, Elsevier.

provided that the gas channel is effectively drained at an adequate rate. For most carbon papers, relatively low capillary pressures and electrowetting effects constrain the flow-by regime, making it difficult to maintain fluid phase separation at commercially relevant current densities (≥ -200 mA cm^{-2}), reducing the FE. In contrast, the carbon cloth GDE maintains high CO_2 reduction performance even under electrolyte flooding, owing to its bimodal pore structure (Fig. 10c). When subjected to pressure differentials equivalent to a 100 cm height, it sustains an average FE for CO of 69% at a current density of 200 mA cm^{-2}, despite continuous liquid breakthrough. When flooding occurs, the electrolyte first fills the larger pores, which are located between the bundles of carbon fibers. These larger pores are more accessible and easier to drain. The liquid tends to exit through these larger pathways before infiltrating the smaller pores within the bundles, which are more critical for gas transport. As a result, a considerable portion of the pore structure remains accessible for gas transport, sustaining electrochemical activity (Fig. 10c). Therefore, CO_2 electrolyzers with carbon cloth GDEs are well-suited for scale-up, as they offer high eCO_2R efficiency while accommodating a wide range of flow regimes.[62] Großeheide *et al.* presented a falling film design (Fig. 10d) to reduce the hydrostatic pressure in catholyte-based electrolyzers. This helped to establish a constant pressure between the gas and liquid sides over the height of the electrode, reducing the pressure difference in the electrolyte channel and mitigating instabilities at the multiphase boundary inside the GDE.[31]

Carbon-based GDEs for large-scale commercial product formation still possess significant challenges.[17] While current density, FE, and catalyst activity have reached acceptable rates for industrial applications, only limited long-term stability has been reported.[30] Therefore, novel approaches utilizing non-carbon GDLs are being actively explored by scientists.[17] However, there is still room for significant advancements in electrode engineering to achieve optimum performances for industrial applications. Baumgartner *et al.*, assessed the feasibility of adopting carbon-free GDEs for eCO_2R. They compared the performance of carbon-free GDEs (97 wt% Ag, 3 wt% PTFE) with typical carbon-based GDEs. The impact of electrowetting on electrochemical performance was studied by evaluating FE for CO at an industrially relevant current density (Fig. 10e). It was found that electrowetting could lead to performance issues in carbon-free GDEs. Until this challenge is addressed, carbon-free GDEs may not yet be able to match the performance of traditional carbon-based GDEs when used as cathodes in CO_2 electrolysis.[30]

Several PTFE GDE scale-up concepts have been proposed recently. Presenting an alternative to carbon-based GDEs, Silva *et al.* developed mesh GDEs consisting of a novel, scalable type of mesh-GDL for CO_2 reduction at high current densities without mass transportation limits (Fig. 10f). They have designed a sandwich-structured electrode (Cu_{mesh}–$PTFE_{filter}$–Cu_{mesh}) composed of a continuous layer of Cu mesh (Cu_{mesh}) interfaced with a PTFE filter. This structure effectively increases flooding resistance without compromising conductivity, with a reported eCO_2R activity of up to -500 mA cm^{-2}. Its metallic structure enables the conduction of large currents and provides enhanced durability due to its capacity to readily undergo *in situ* oxidation–reduction cycles. Furthermore, the study finds that high partial current densities can be achieved by increasing mesh sizes, while morphological changes and reaction-driven electrolyte contamination remain critical factors for maintaining steady performance, even when flooding is mitigated.[17]

Even though PTFE has been introduced to prevent flooding, in-plane resistance due to the low conductivity of PTFE-based GDEs has hindered scalability.[8,20] The size of this type of electrode has been limited to 1–5 cm^2, as electrical current is delivered through edge contacts that rely solely on the in-plane conductivity of the thin catalyst layer. In the case of thick catalyst layers, it must be ensured to have sufficient in-plane conductivity.[8] Overcoming this challenge, novel current collectors have been designed to enable scale-up.[20] Filippi *et al.* have proposed a novel multifunctional metallic current collector design that allows direct, multipoint front contact of catalyst layers coated on PTFE-based cathodes, facilitating the reliable scale-up of PTFE-based GDEs to $\geq$100 cm^2 (Fig. 11a). This helps minimize performance losses, even in cathodes with high resistivity. The flow-field functionality in a monopolar plate configuration effectively reduces the electrolyte gap distances to enhance system performance. This design significantly advances the development of larger CO$_2$ electrolyzers for scale-up processes while maintaining high FE in eCO$_2$RR.[8]

5.1.2 Microenvironment tuning. The microenvironment at the electrode–electrolyte interface during electrocatalysis also plays a vital role as electrocatalytic reactions occur in the nanoscale space at this electrified interface.[141] Interface engineering and electrolyte optimization serve as effective microenvironment tuning strategies, enabling precise control over local physicochemical parameters. To enhance the efficiency of the eCO$_2$R process, surface modification at the electrode–electrolyte interface using compounds such as solvated alkali metal ions, charged organic surfactants, and polymers have been investigated. Such modifications play a key role in regulating the interfacial properties, especially the charge distribution and hydrophobicity. For instance, electrocatalysts can be modulated using anionic and non-ionic surfactants. To induce surface modifications, the anionic surfactant sodium dodecyl sulfate can be employed, as it influences the dispersion and morphological characteristics of electrocatalytic particles. In nanomaterial synthesis, non-ionic surfactant polyvinylpyrrolidone can be used as a capping agent to stabilize the structure, maintain the defined morphology, avoid particle agglomeration, and mitigate irregular growth.[22] Furthermore, to enhance the highly active catalytic regions, creating a semi-hydrophobic microenvironment within the catalyst layer is crucial. To achieve this, researchers have explored the incorporation of rigid colloids, such as PTFE or SiO$_2$, into the catalyst layer.[20] CO$_2$-phil microgels with amine moieties in their structure are another compound added to the catalyst layer to tune the microenvironment. They differ from commonly used colloids and possess highly tunable physical and chemical properties, high CO$_2$ storage capability, and a 3D structure that creates well-constructed triple-phase interfaces. These unique properties facilitate the increase of local CO$_2$ concentration, leading to enhanced reaction rates.[20] Rabiee *et al.* have utilized the rational design of CO$_2$-phil microgels with pyridine-based amine moieties to tune the microenvironment of PTFE-based GDEs for ethylene production (Fig. 11b). This facilitates improved CO$_2$ availability, enabling stable selectivity at high current densities

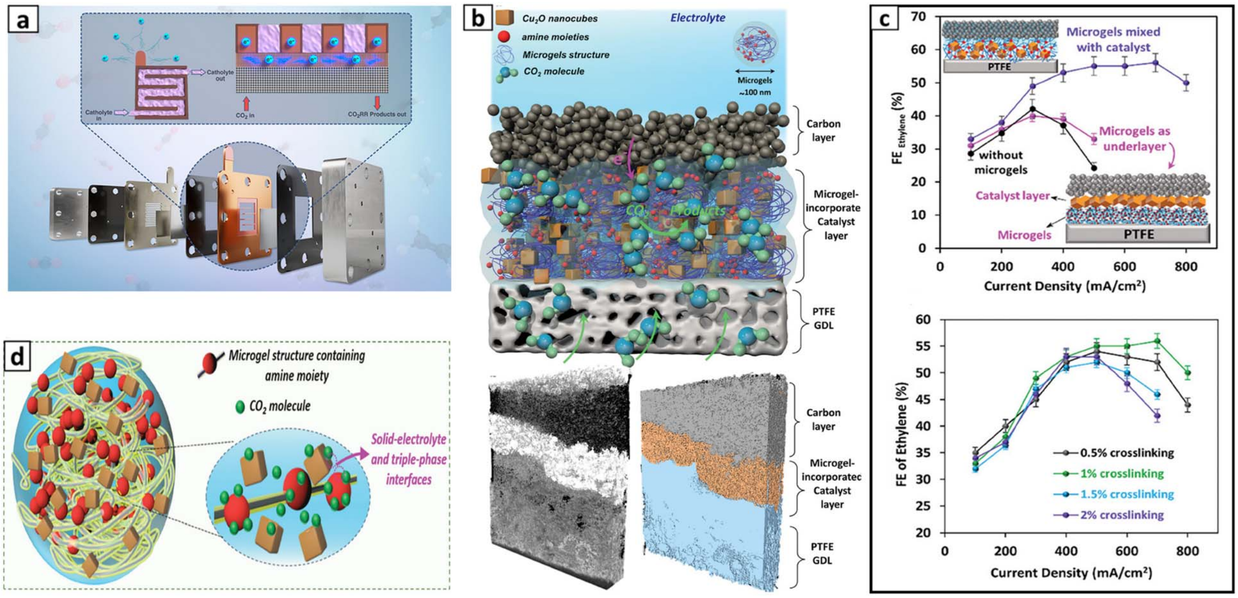

Fig. 11 (a) The cell design with the monopolar plate current collector. Reproduced with permission.[8] Copyright 2024, American Chemical Society. (b) Schematic illustration of the GDE consisting of a catalyst layer, modified with microgels, and a carbon black top-layer on the PTFE substrate. (c) Effect of microgel addition and the geometry of microgel addition to the GDE (upper) and microgel crosslinking ratio on ethylene selectivity (lower). (d) Schematic illustration depicting the formation of triple-phase boundaries and the solid–electrolyte interface in the microgel 3D structure and proximity of the catalyst. Reproduced with permission.[20] Copyright 2024, Wiley-VCH Verlag GmbH & Co. KGaA, Weinheim.

(700 mA cm^{-2}) and the increased FE (56%) for ethylene production compared to GDEs without microgels (Fig. 11c). These favorable observations can be attributed to the heterocyclic amine backbones in the microgels, which serve as CO_2 micro-reservoirs within the catalyst layer, enhancing CO_2 availability. Further, due to 3D structure, CO_2 availability and catalytic activity are balanced through the crosslinking ratio of the microgels (Fig. 11d).[20]

Optimizing the electrolyte composition can also influence the eCO_2RR.[142] Surfactants can be utilized to refine the electrolyte composition. This enables effective regulation of ion distribution and optimizes the CO_2/H_2O ratio, thereby enhancing mass transfer at the electrode–electrolyte interface. For example, dodecylphosphonic acid and its analogues modulate the interfacial H-bond environment on Ag nanoparticle electrodes. These surfactant additives promote the hydrogenation of CO_2 to *COOH, increasing CO production and suppressing the kinetics of HER.[22] Another important surfactant is cetyltrimethylammonium bromide (CTAB), which facilitates enhanced charge transfer and increased local CO_2/H_2O ratio. Under an external potential, CTAB molecules are absorbed onto the electrode surface, forming a dense layer with a hierarchal structure through charge interactions. Particularly, this ordered assembly at the electrode–electrolyte interface regulates the interfacial water, thereby creating a hydrophobic microenvironment that limits the local proton availability for the HER.[22,141] Further, the energy barrier of *CO desorption is significantly reduced.[22] Therefore, the effect of CTAB on charge transfer and HER suppression was studied by Kuang *et al.* They utilized Ag HFGDEs (Fig. 12a) to investigate this phenomenon by introducing CTAB as the electrolyte additive to modulate the microenvironment at the electrode–electrolyte interface. Their results demonstrated that due to the CTAB additive, GDE can be operated in a wide potential range at high current densities for CO production and achieved FE > 90%. These enhanced performances are attributed to the ordered arrangement of hydrophobic long-alkyl chains in CTAB molecules at the electrode–electrolyte interface, which facilitates CO_2 transport to the active sites while repelling water, thereby suppressing the competing HER.[22]

Incorporating halide ions into the electrolyte solution significantly enhances catalyst performance by forming a structured layer on the electrode surface. This process optimizes the local electronic environment and promotes the adsorption of key intermediates, thereby improving eCO_2R performance.[142] This phenomenon will be further discussed in Section 5.2.4. Most reduction reactions are carried out under strongly alkaline conditions.[130] GDEs operating in alkaline aqueous electrolytes demonstrate high activity and selectivity towards target products (such as CO), and this is attributed to

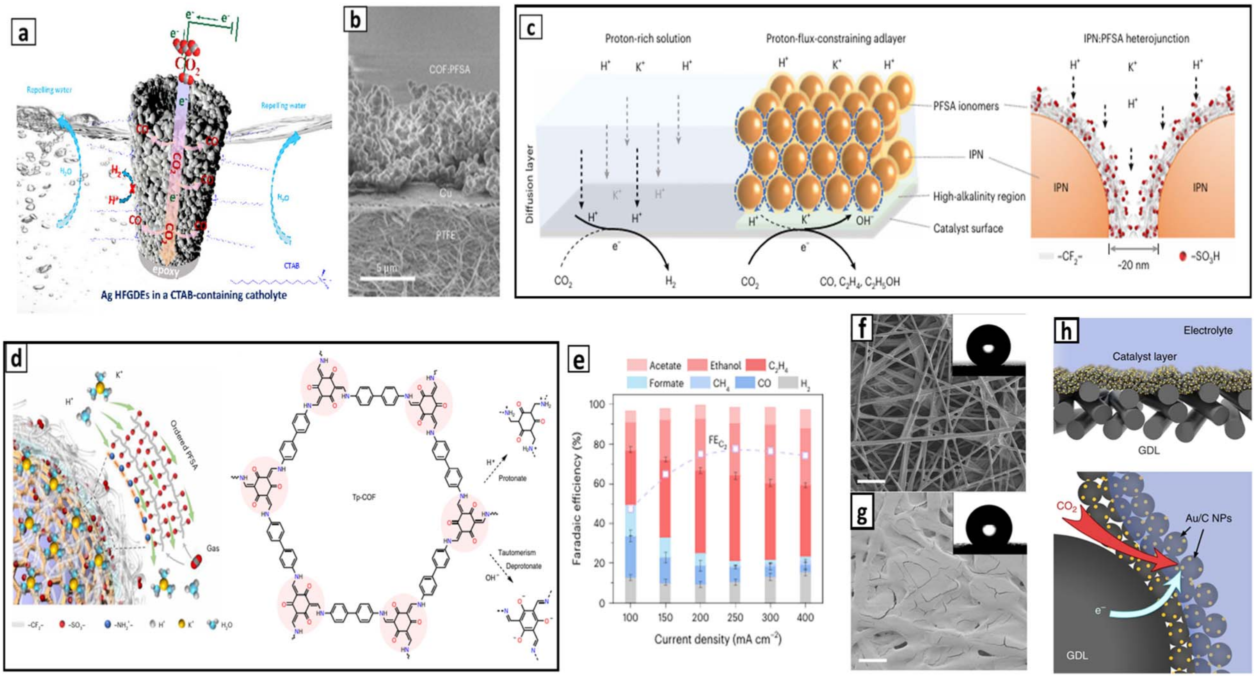

Fig. 12 (a) Ag HFGDE in a CTAB containing catholyte. Reproduced with permission.[22] Copyright 2024, Wiley-VCH Verlag GmbH & Co. KGaA, Weinheim. (b) Cross-sectional SEM image of covalent organic framework-PFSA adlayer on PTFE–Cu substrate. (c) Schematic illustration of interfacial reactions and proton transport dynamics near the catalyst surface. (d) Schematic illustration of the functionalized covalent organic framework designed to regulate ionomer structure and the transport of ions and gases in the catalyst microenvironment (left) and amphoteric covalent organic framework structure and its sensitivity to changes in surrounding acidity (right). (e) FE of various products at different current densities. Reproduced with permission.[147] Copyright 2023, Springer. (f) SEM image of the PTFE-modified carbon fibre GDL. (g) SEM image of the electrode after coating with an Au/C nanoparticle film. (h) Schematic illustration of the three-phase contact electrochemical cathode (above) and the gas–liquid–solid three-phase interfaces of a three-phase contact system for eCO_2RR (below). Reproduced with permission.[36] Copyright 2020, Springer.

reduced ohmic drops,[21,143] favorable electrode kinetics,[65,144] and suppression of water electrochemical reduction as a side reaction.[145] However, planar GDEs operating under alkaline conditions are prone to carbonation-derived blockage and reduction in hydrophobicity, resulting in flooding, particularly at high current densities, affecting eCO_2RR and catalyst stability.[130,146] The significant non-faradaic consumption of CO_2 in alkali electrolytes limits CO_2 diffusion and mass transfer.[130] To address this, investigations have been conducted on optimizing the structure and micro-environment of electrodes, including factors such as layer thickness, electric field, and pressure, to enhance the effective CO_2 concentration at interfaces.[48] However, exploring gas–liquid–solid three-phase interfaces is difficult due to the limited understanding of interfacial structures and CO_2 transport behavior under nonequilibrium conditions. This is due to the necessity of simultaneously considering the rate of CO_2 consumption by electrochemical reactions and the supply of CO_2 from the bulk to the electrode surface.[36]

Moreover, the loss of CO_2 reactants can also be identified as a major challenge in neutral electrolytes. Therefore, acidic electrolytes offer a potential solution to addressing these issues. However, the proton-rich environment near the catalyst surface promotes the HER, reducing the energy efficiency for multicarbon product formation. Mitigating the above problems, Zhao *et al.* have reported a method to control the catalyst microenvironment in strongly acidic conditions, achieving FE 75% for multicarbon product formation at 200 mA cm^{-2}. They employed a heterogeneous catalyst adlayer consisting of covalent organic framework nanoparticles and cation-exchange ionomers (perfluorinated sulfonic-acid (PFSA)) (Fig. 12b). The catalyst adlayer limits proton influx at the catalyst–electrolyte interface, enhancing local alkalinity (pH > 11) to favor C_2 product formation while maintaining effective ion conductivity (Fig. 12c). The imine and carbonyl-functionalized covalent organic framework structures modulate the ionomer arrangement, forming uniformly distributed cation-carrying and hydrophilic–hydrophobic nanochannels (Fig. 12d).[147] This composite structure restricts proton transport to the hydrophilic nanochannels and promotes the accumulation of potassium ions at the catalyst surface, enabling a kinetically favourable local environment for efficient CO_2 activation ($FE_{eCO_2R} > 85\%$) while suppressing HER ($FE_{H_2} < 15\%$) (Fig. 12e).[147] Furthermore, researchers have focused on achieving efficient CO_2 conversion at ampere-level current densities by tailoring the CO_2 electrocatalytic microenvironment through three-phase interface engineering.[142]

The wettability of gas–liquid–solid interfaces is another crucial factor to consider, attracting significant interest as the surface wettability of electrodes is intimately related to the catalytic rate of various electrochemical reactions that involve gas-phase reactants.[72,148] Changes in wettability across gas–liquid–solid interfaces can significantly alter gaseous reactants and products transportation and the interaction between catalytic sites and electrolyte ions. These variations play a crucial role in influencing gas diffusion and electron transfer processes, which are key factors determining the kinetics of electrochemical reactions.[149] Therefore, for the rational design of more efficient eCO_2R systems, exploring wettability control to simplify the complex variables in three-phase contact systems is essential. This approach enables investigation into the relationships among interfacial structures, CO_2 transport, and CO_2 electroreduction.

In this regard, Shi *et al.* demonstrated the impact of wettability on eCO_2R using a typical Au/C electrode model. The PTFE-modified carbon fiber paper with an external water contact angle of 151 ± 2° has been employed as a superhydrophobic porous GDL (Fig. 12f). The catalyst layer with an average thickness of 1.2 ± 0.1 μm was fabricated by applying Au/C nanoparticles as a thin film (Fig. 12g). The catalyst layer was supported by the carbon fibers while preserving the internal pores of the GDL unobstructed. This architecture is vital as it enables the rapid and continuous transport of gaseous CO_2 from the bulk gas phase to Au active sites through the porous electrode. It demonstrated the Cassie–Wenzel coexistence wetting state which is the ideal interface structure for eCO_2R that maintains 80% of the initial CO_2 concentration at the interface, operating at current densities above 100 mA cm^{-2}. This caused enhanced stable interfacial CO_2 transport in high current densities and ensured effective contact between catalytic active sites and the electrolyte.[36]

Furthermore, their research findings highlighted that in three-phase contact systems (Fig. 12h), the efficiency of eCO_2R at high current densities is significantly affected by the CO_2 concentration at interfaces. This concentration is primarily controlled by the efficiency of CO_2 mass transfer across interface structures. Facilitating the efficient transport of CO_2 from the bulk phase to the optimized three-phase interfaces is critical for stabilizing the non-equilibrium CO_2 concentration at interfaces. This is essential for achieving effective CO_2 reduction performance at high current densities, minimizing diffusion limitations.[36]

5.2 Transition to HFGDEs and their progress

Although the typical planar GDEs are adopted over traditional planar electrodes (including mesh electrodes)[130] to enhance the mass transport at the reaction interface through concentration diffusion, enabling efficient eCO_2RR, the subtle triphasic interface configurations still lead to limited performance stability. As discussed in previous sections, this instability is often mainly due to mass transfer degradation caused by flooding and salting out, hindering their practical scale-up.[150] Further, traditional planar GDEs, which consist of multiple components, intricate configurations,[151,152] and additional device support,[130] are difficult and complex to fabricate.[151–153] Complex manufacturing procedures require different steps for GDL and catalyst layer and restrict the active area by the electrochemical reactor's size. Increasing the electrolyzer's area in such systems typically requires adding more GDE stacks in a multilayer configuration.[154] This complexity can limit their potential for large-scale use.[151–153] Additionally, the binders used in these electrodes may degrade over time during long-term electrolysis, negatively affecting the stability and performance of CO_2 reduction.[56,152] Therefore, there is a need for more robust and easier-to-manufacture GDEs.[152]

In recent years, researchers have paid increased attention to the different geometric architectures of GDEs to overcome the limitations associated with planar GDEs. In this regard, hollow fiber (microtubular) GDEs, which are self-supported three-dimensional GDEs with gas penetration structures,[130] have emerged as a promising alternative for CO_2 electroreduction,[154,155] addressing some of these challenges.[154] This tubular design offers a significantly higher surface area[100,154,156] compared to planar GDEs having the same volume,[154] enabling the effective loading of diverse and dense electrocatalysts for eCO_2RR,[25] making them well-suited for large-scale applications[22] and rich three-phase boundary for gas–liquid reactions,[130,156] unique three-dimensional porous structure promoting efficient mass transfer *via* flow-through modes,[130,157] and simplified component.[130] Further, it facilitates the increased local CO_2 concentration and inhibits the flooding effect due to the bilateral pressure difference of the hollow fiber wall, leading to forced CO_2 diffusion to the active sites.[130] Most importantly, the unidirectional mass transfer in HFGDEs prevents the development of carbonate blockage of gas transmission channels under strongly alkaline conditions, which would otherwise significantly limit CO_2 diffusion.[130] Considering the different electrode structures that emerged for eCO_2R from planar electrodes and 3D electrodes with special shapes (*e.g.*, tubular electrodes, spherical electrodes, and hollow fiber electrodes) to planar GDEs and HFGDEs, the HFGDE has been identified as the most promising candidate so far for enabling industrial applications of eCO_2R. This relevance primarily stems from their mature fabrication technique, stable and robust unitized configuration, porous structure, and adjustable

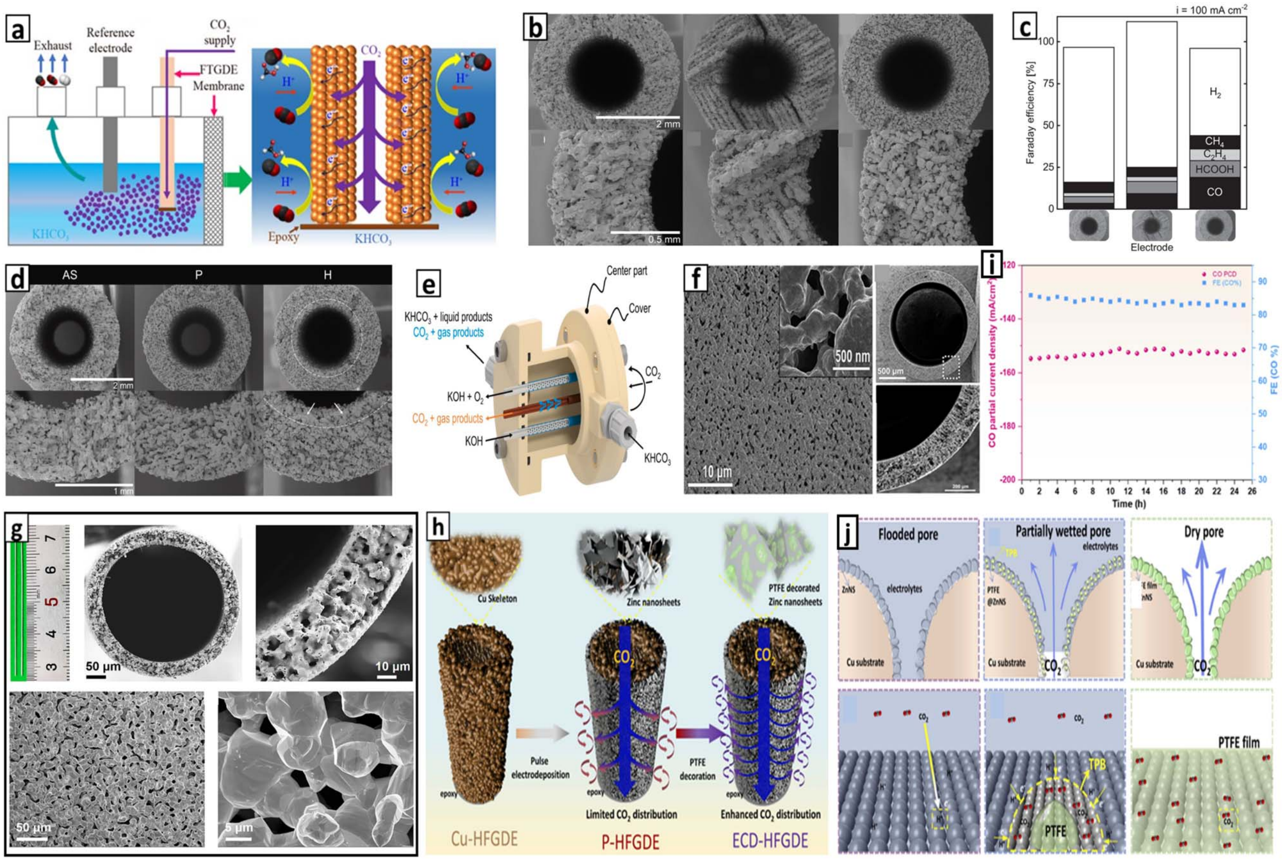

Fig. 13 (a) Schematic illustration of the Cu flow-through GDE system for CO_2 electroreduction (left), CO_2 diffusion and electrochemical conversion of CO_2 within the GDE (right). Reproduced with permission.[159] Copyright 2024, Springer. (b) Cross sectional view (above) and close-up view (below) of different electrodes. (c) FE of different electrodes for several products at the current density of 100 mA cm^{-2}. Reproduced with permission.[161] Copyright 2023, Wiley-VCH Verlag GmbH & Co. KGaA, Weinheim. (d) Cross-sectional views of almost solid (AS), porous (P), and hybrid (H) electrodes, respectively, from left to right. (e) Reactor configuration and associated material flow paths in flow-through (blue) and flow-by (orange) operation modes. Reproduced with permission.[155] Copyright 2024, Elsevier. (f) Morphology of Cu hollow fiber; SEM image of the outer surface (left) and cross-section SEM images (right) with low (upper) and high (lower) magnification. Reproduced with permission.[152] Copyright 2021, Elsevier. (g) Morphology of Ag hollow fiber; optical image and SEM images of cross-sections (upper) and SEM images of the outer surface (below). Reproduced with permission.[99] Copyright 2022, MDPI, Basel, Switzerland. (h) Schematic illustration of the preparation of enhanced CO_2-distributed HFGDE (P-HFGDE is pristine 2D Zn nanosheets deposited Cu hollow fiber, and ECD-HFGDE is enhanced CO_2-distributed HFGDE). (i) FE and partial current density for CO within 26 h. (j) Flooded pores (upper) and CO_2 transportation and eCO_2RR with dissolved CO_2 (lower); partially wetted pores (upper) and CO_2 transportation and eCO_2R in optimized triple-phase boundaries (lower); and dry pores (upper) and eCO_2R in gas–catalyst interfaces (lower). Reproduced with permission.[25] Copyright 2025, Elsevier.

shape.[130] Particularly, HFGDEs featuring a porous hierarchical wall can modulate the triple-phase reaction zone, thereby enhancing the performance of eCO_2RR.[158] The need for a separate gas chamber in planar GDEs has been effectively addressed by HFGDEs, which utilize the lumen side of the hollow fiber as the gas chamber. This facilitates the direct feeding of CO_2 into the inner chamber, allowing it to penetrate through the hollow fiber walls and supply sufficient CO_2 near the catalyst.[103]

Various research groups have focused on developing HFGDEs to enhance their electrocatalytic performance by improving selectivity at high current densities, promoting eCO_2RR efficiency while suppressing the competing HER, and facilitating efficient mass transfer of reactants to the catalyst surface.[155] Mustafa *et al.* utilized GDEs with tubular architectures to enhance reaction kinetics. This approach increased the local CO_2 concentration and enhanced the triple-phase interface, providing abundant electroactive sites for achieving superior reaction rates.[159] Their strategy involved efficient formate production through robust and self-supported Cu flow-through GDEs (Fig. 13a). The reported high formate FE (76%) and current density (265 mA cm^{-2}) at −0.9 V *vs.* RHE in 0.5 mol L^{-1} are attributed to the porous structure of Cu flow-through GDEs. Further, stable operation over several hours has been achieved through the combined phase inversion and calcination process.[159] Economically viable GDE designs have become increasingly important for the commercialization of eCO_2R technologies. In this regard, as a cost-effective alternative to noble-metal catalysts for CO production, Liu *et al.* developed an architecturally optimized Zn HFGDE. The distinctive penetration effect of this electrode facilitated local CO_2 enrichment and rapid replenishment at the active sites, achieving a CO FE exceeding 90% and maintaining stable operation for 110 h at a current density of 800 mA cm^{-2}.[160] The fundamental structure of HFGDEs has undergone significant architectural modifications to overcome challenges and achieve more efficient CO_2 reduction performance. The subsequent discussion highlights the major advancements underlying these structural innovations.

5.2.1 Pore structure modelling.

The unique penetration effect that forces CO_2 to disperse and penetrate through the abundant pores on the HFGDE wall,[150] leads to enhanced interface reactions and oriented mass transfer.[142,150] This aspect has given much attention when exploring industrial scale applications targeting enhanced eCO_2RR kinetics by overcoming mass transfer limitations.[150] Therefore, precise manipulation of pore structure is crucial. The inhomogeneous pore geometry of HFGDEs presents challenges, leading to poor CO_2 distribution and, consequently, limited current density due to poor reaction kinetics and competing HER. Tuning the pore structure and post-treatment strategies can be used to address this issue. However, tuning the pore architecture of HFGDEs is a complex process that requires balancing multiple parameters of the fabrication process (*e.g.*, the ratio of polymer binders to metal powders, the type and size of metal powders, and the sintering temperature and duration), and post-treatment stands out as a promising strategy. Moreover, this approach facilitates modulation of the electrode wettability, enabling more uniform CO_2 delivery, higher current density, and improved eCO_2R activity.[25] To boost the eCO_2RR while mitigating the competing HER, Weber *et al.* developed tubular copper GDEs fabricated *via* selective laser melting (SLM). The porosity, pore diameter, and electrochemically active surface area of the generated pore network were tailored using the laser hatching strategy (Fig. 13b). Their findings revealed that modifying the pore network structure has a direct impact on the eCO_2RR, leading to approximately a 30% reduction in competing HER (Fig. 13c). Therefore, a dominant eCO_2R process was reported at current densities of 100 mA cm^{-2}.[161]

In another study, Weber *et al.* explored tubular 3D printed Cu GDEs (solid, porous, and hybrid porous) in a continuous flow reactor to control the mass transfer by manipulating flow conditions. They studied the effect of GDE wall thickness and evaluated different electrode arrays to identify favorable layouts (Fig. 13d). Moreover, they studied the effect of gas supply on catalyst performance: the flow-through mode, where CO_2 is actively forced through the porous electrode walls, and the flow-by mode, in which diffusion is the governing transport mechanism (Fig. 13e). The hybrid porous electrodes in flow-through mode demonstrated superior performance due to enhanced CO_2 mass transfer to the catalyst surface. In flow-by mode, electrodes exhibited reduced performance dominating HER, likely caused by the substantial electrode wall thickness and prolonged diffusion pathways. They successfully operated the reactor at high current densities, reaching up to 500 mA cm^{-2}.[155]

Utilizing a phase-inversion/sintering process, Zhu *et al.* have reported a Cu hollow fiber of GDE for formate production with a FE of 80% at high current density (210 mA cm^{-2}) and high yield compared to other Cu structures (*e.g.*, foil and foam). This Cu hollow fiber, composed of metallic Cu with hierarchical pore structures, provides a robust self-supported GDE without any binder (Fig. 13f).[152] The hierarchical morphology enhances mass transfer and the exposure of active sites.[162] By forcing CO_2 molecules to penetrate through the porous wall, CO_2 activation and strong interactions with the active sites are achieved, promoting formate production.[152] Li *et al.* also used this strategy of forcing CO_2 through porous electrode walls for better penetration utilizing gas flow-through configuration. They developed a silver hollow fiber electrode (Fig. 13g) as a novel self-supported GDE for efficient and stable CO_2 electroreduction to CO with excellent electrocatalytic performances, suppressing competitive HER and facilitating CO_2 reduction kinetics. The reported FE of over 92% at current densities above 150 mA cm^{-2} was achieved in 0.5 M $KHCO_3$ for over 100 h. These favourable observations can be ascribed to the unique pore structures, which provide abundant active sites and efficient mass transport.[99]

Pore accessibility is a critical factor for GDEs, and pore utilization can be enhanced by controlling the wettability through pore structure modification. Chen *et al.* have developed a facile strategy to enhance CO_2 distribution and the triple-phase boundary formation. Their approach involved incorporating a hydrophobic agent (*e.g.*, PTFE) to reduce pore blockage and enhance pore utilization for gas diffusion, leading to reduced pore capillary pressure and enhanced CO_2 distribution (Fig. 13h). 5 wt% PTFE water solution treatment was applied to pristine 2D Zn nanosheets deposited Cu hollow fiber, resulting in improved current density and FE for CO (Fig. 13i). This can be ascribed to the reduction in the number of flooded pores and the enhancement of CO_2 distribution due to optimal electrode wettability (Fig. 13j).[25]

5.2.2 **Surface engineering.** The surface reconstruction of electrocatalysts in HFGDEs is a facile strategy to enhance the efficiency of eCO_2R. This has been studied by Kuang *et al.*, developing a porous microparticle Ag-based HFGDE *via* an *in situ* electrochemical oxidation–reduction method. They have reported good performance with FE of 94% for CO and a partial current density of 83.4 mA cm^{-2}. These favorable outcomes can be attributed to surface reconstruction, which lowers the activation energy barrier of the rate-limiting step in the initial electron/proton transfer.[158] Further, nanoengineering of electrocatalysts is a highly effective strategy for modulating the eCO_2RR pathway and tailoring product selectivity.[163] Utilizing this technology, Chen *et al.* have developed HFGDEs with zinc crystal facets controlled nanosheet catalysts for syngas production (Fig. 14a).[101] The production of syngas requires a dual-active-site catalyst capable of simultaneously promoting the HER and the electrocatalytic conversion of CO_2 to CO.[101,164] To regulate the syngas ratio, the facet control of metal or metal oxide electrocatalysts is an effective method. Zn, in particular, is a strong candidate for syngas generation by adjusting the proportion of Zn (101) to Zn (002) facet.[165] The Zn (101) facet is favoured for CO production, as it exhibits a lower energy barrier for eCO_2RR and a higher energy barrier for the HER. In contrast, the Zn (002) facet predominantly facilitates HER.[166] Using CTAB, a controllable, facile surfactant-assisted method was employed to electrodeposit the facet-oriented Zn nanosheet catalyst on the Cu HFGDE. CTAB influences the nucleation and crystal growth of Zn ions on the GDE during the electrodeposition process, resulting in controlled modifications of surface free energy and tuned Zn crystal growth orientation. A current density of 73.3 mA cm^{-2} and a high syngas production rate of 1328.6 µmol h^{-1}

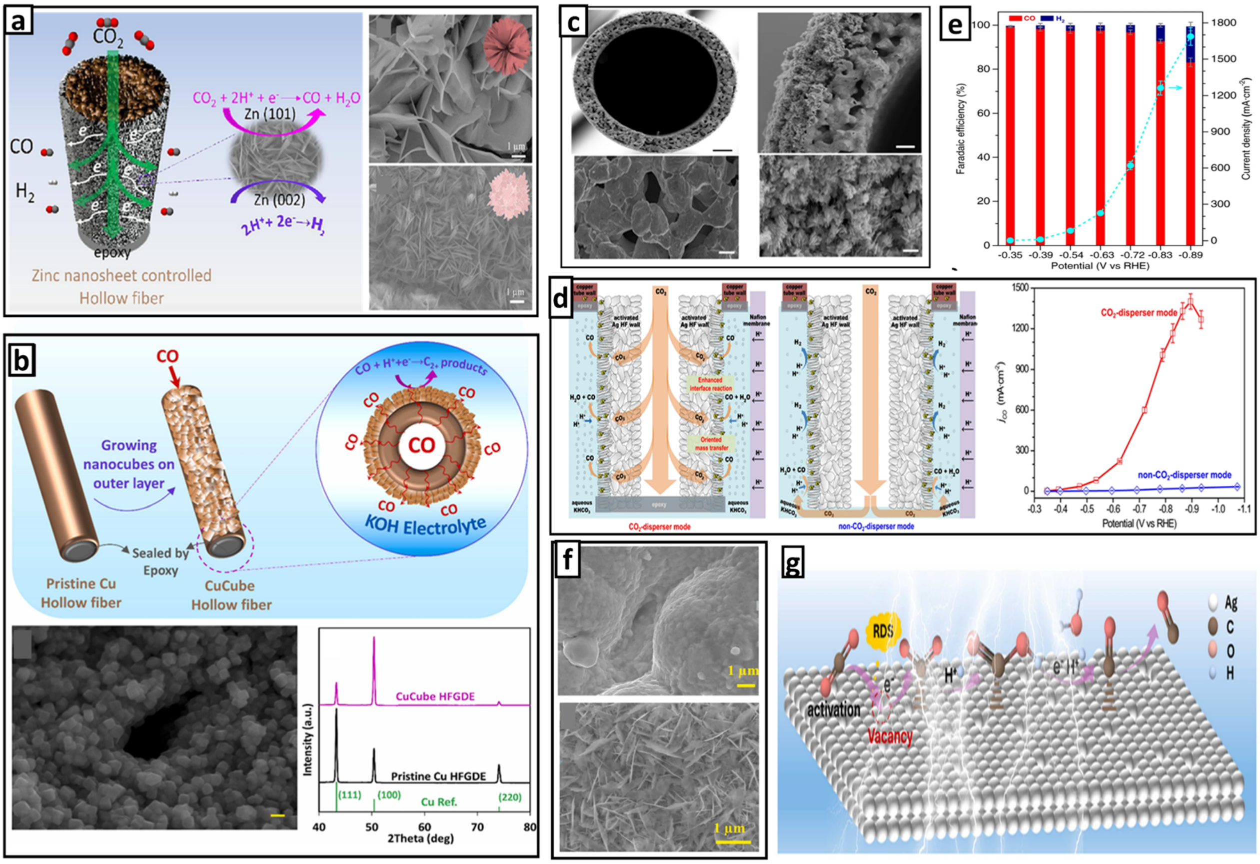

Fig. 14 (a) Zn nanosheet-controlled HFGDE (left) and SEM images (right) of Zn nanosheet hollow fiber (upper) and Zn-controlled nanosheet hollow fiber (below). Reproduced with permission.[101] Copyright 2024, Elsevier. (b) Schematic illustration of HFGDEs and growing nanocubes on the outer layer (upper), FESEM image of Cu cube HFGDE with nanocubes covering the surface and XRD of pristine and Cu cube HFGDEs, respectively (lower). Reproduced with permission.[97] Copyright 2023, Elsevier. (c) SEM images of cross sections of Ag hollow fiber and activated Ag hollow fiber, respectively (upper), and SEM images of the outer surface of Ag hollow fiber and activated Ag hollow fiber, respectively (below). (d) Schematic illustration of CO_2-disperser mode, the non-CO_2-disperser mode, and CO partial current densities at the two modes, respectively. (e) FE for CO and H_2, and total current densities over the potential range of −0.35 to −0.89 V. Reproduced with permission.[153] Copyright 2022, Springer. (f) SEM images of surfaces of Ag HF (upper) and defect-rich silver nanosheets HF (lower). (g) Reaction pathway of the CO_2 conversion into CO on defect-rich silver nanosheets HFGDE. Reproduced with permission.[170] Copyright 2025, Elsevier.

cm^{-2} were achieved, attributed to the sufficient CO_2 supply at the catalyst/electrolyte interface, facilitated by the hierarchical structure of the HFGDE and the abundant active sites provided by the well-connected zinc nanosheets.[101]

The flow-through gas delivery configuration allows the gas to be in complete contact with the electrolyte on the outer layer of HFGDEs, causing the interactions between CO_2 and OH^-. This has resulted in the application of HFGDEs for eCO_2RR being restricted to non-alkaline electrolytes. However, this limitation is unlikely in CO reduction reaction due to the inherent stability of CO in alkaline media and is expected to achieve high current densities.[97] Furthermore, the migration of CO_2 to the anode side as carbonates causes CO_2 loss.[167] CO is the key reaction intermediate towards C_{2+} compounds for eCO_2RR, with high selectivity, reaction rates, and improved stability. The electroreduction of CO_2 to CO is much more effective and is being commercially deployed.[150] CO production through eCO_2R is regarded as one of the most promising processes in the chemical industry due to its favorable technical and economic feasibility.[168] These facts have established CO reduction as a promising approach for C_{2+} production following CO_2 reduction to CO.[97] The two-step conversion of $CO_2 \rightarrow CO$ and $CO \rightarrow C_{2+}$ products offers several advantages over direct CO_2 electrolysis to C_{2+} products. In the CO-to-C_{2+} conversion process, formic acid and CO, which interfere with C_{2+} production in eCO_2RR, are not generated.[169] Rabiee *et al.* have developed Cu-based HFGDEs for efficient CO reduction to C_{2+} products by tuning the Cu catalyst shape morphology and promoting the orientated growth of nanocubes on the outer surface of HFGDEs through electrodeposition (Fig. 14b). High current densities (>470 mA cm^{-2} for ethylene) and FEs of C_{2+} products (>90%) were achieved in 1.0 M KOH electrolyte. These outstanding performances were attributed to the efficient C–C coupling and the high C_{2+} selectivity of copper nanocubes with dominant Cu (100) lattice facet.[97]

Even though HFGDEs have provided the best configuration for the eCO_2R process to achieve economically viable electrochemical CO_2 conversion, they still offer limited current densities ($\leq$200 mA cm^{-2}).[98] To achieve stable high current densities, Li *et al.* developed an HFGDE with hierarchical micro/nanostructures composed of metallic silver (Ag) through electrochemical redox treatment to rearrange the ordered nanorods on the surface (Fig. 14c). It acts as a CO_2 disperser (Fig. 14d), enhancing three-phase interface reactions and mass transfers due to the interactions between CO_2 and the active site of the hollow fiber wall while penetrating through the hollow fiber wall under a limited gas diffusion environment.[153] Optimizing the CO_2 transport channel on the surface of HFGDEs is a practical approach to improving reaction efficiency, as the surface structure of the hollow fiber strongly influences CO_2 mass transfer.[130] The reported modified Ag HFGDEs exhibited high FE for CO (~93%), a high current density of ~1.26 A cm^{-2} at the potential of −0.83 V (*vs.* RHE) (Fig. 14e), and extended longevity (168 h).[153] Further, the surface structure and composition significantly affect the active area, catalytic capacity, product selectivity, yield, and formation path of products. Different electrodeposition methods can achieve different surface structures, and post-treatment processes can be used to form varying electrode components.[130]

At varying current densities, factors such as catalyst activity and CO_2 availability influence the eCO_2R process differently. Understanding these effects is crucial when designing GDEs, particularly for applications aimed at industrial-scale implementation. The catalyst activity primarily controls eCO_2RR performance at lower current densities, whereas sufficient CO_2 supply becomes critical for sustaining high selectivity and suppressing the HER under industrial conditions. To study this, Chen *et al.* developed HFGDEs with *in situ* grown, defect-rich silver nanosheets (Fig. 14f). They reported a CO partial current density of 381.8 mA cm^{-2} at a total current density of 500 mA cm^{-2}. The abundant defect sites in the silver nanosheets enhance CO production by stabilizing the *COOH intermediate (Fig. 14g), and the HFGDE configuration ensures sufficient CO_2 delivery to the active sites.[170]

In further studies, researchers found that as wettability critically affects the microenvironment, a balanced electrode surface with both hydrophilic and hydrophobic regions is best, as it supports proper interaction of all three phases. This is because a superhydrophilic electrode surface can cause excessive wetting of the GDE, leading to pore blockage and flooding of the gas transport layer, whereas a superhydrophobic surface may hinder adequate contact between the electrolyte and the electrocatalyst. In this regard, Rabiee *et al.* proposed an innovative approach to creating distinct wetting regions on a dual-layer HFGDE by depositing a bismuth-embedded carbon nanotube (CNT-Bi) catalyst layer onto a Cu HFGDE (Fig. 15a), enabling efficient CO_2 reduction to formate. Here, *in situ* electrochemical oxidation was employed to modulate the wettability of dual-layer HFGDEs, thereby controlling the extent of electrolyte infiltration into the CNT layer and establishing a dual-region hydrophilic–hydrophobic environment. The current density of ~150 mA cm^{-2} with FE of >90% for formate production (Fig. 15b) was achieved due to the formation of enriched triple-phase interfaces (Fig. 15c), the presence of nanocatalysts, a conductive CNT scaffold, and the generation of finer gas bubbles as the CO_2 passes the CNT layer. The development of hydrophilic–hydrophobic regions within the CNT layer, along with abundant microchannels for CO_2 transport, fosters a well-regulated microenvironment that facilitates the formation of highly efficient triple-phase interfaces.[102]

5.2.3 Alloying. The synergistic effects of alloy catalysts have been employed to enhance the FE and current density of HFGDEs.[171] The efficiency of metal electrocatalysts is closely linked to their valence state, and the presence of oxide species is critical. However, the oxide valence of some metals, like Sn, shows instability under cathodic conditions, leading to a loss in efficient long-term performance. In this scenario, alloy electrocatalysts offer superior physiochemical stability, ensuring sustained performance during prolonged electrolysis. For example, the stability of Sn-coated HFGDEs can be enhanced by synthesizing a selective CuSn (bronze) outer layer on the Cu HFGDE. It improves the selectivity, suppresses the HER, and offers a lower overpotential to achieve optimal product formation.[100] However, with existing methods, such as depositing powder foam alloy

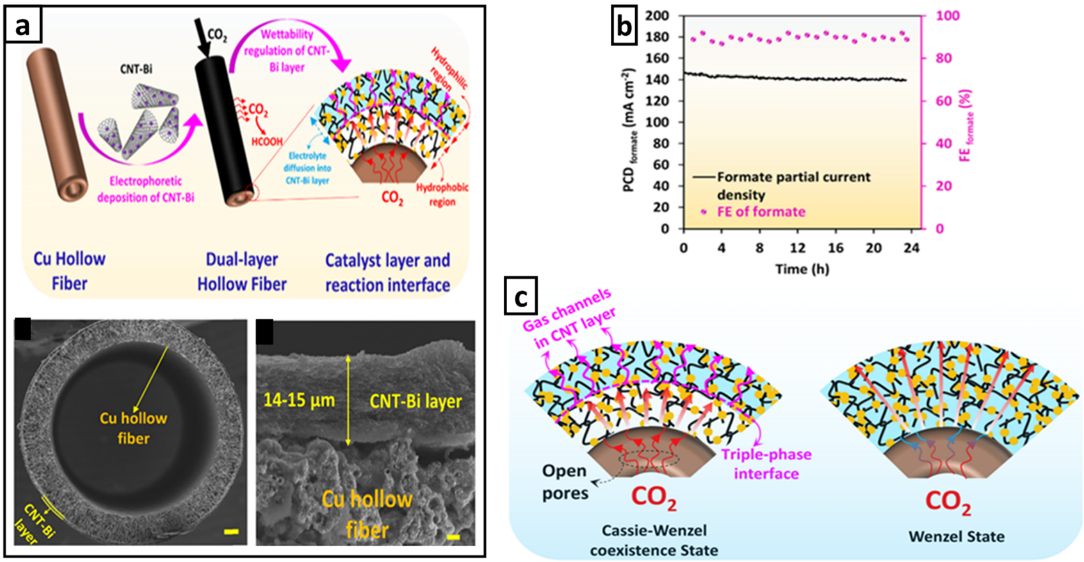

Fig. 15 (a) Schematic illustration of dual-layer HFGDE fabrication and eCO$_2$R process on CNT-Bi layer (upper) and cross-sectional FESEM images of dual-layer HFGDE (below). (b) FE and formate partial current density within 24 h. (c) Schematic illustration of triple-phase interface formation; coexistence of Cassie–Wenzel state and forming the triple-phase interface (left) and Wenzel state – electrolyte wetting of the CNT layer, which may lead to pore blockage (right). Reproduced with permission.[102] Copyright 2022, Elsevier.

catalysts, achieving a self-supporting GDE with a uniform and distinctive alloy coating and strong catalyst–substrate interfacial binding is challenging. This issue arises from several factors, including the difficulty of achieving uniform catalyst powder deposition on HFGDEs with a small diameter, the electrical resistance of the interface of the deposited layer and the GDE substrate, and the use of ionomers (*e.g.*, Nafion), which can block pores and cover active sites, thereby reducing catalytic activity by preventing electrolyte wetting. Rabiee *et al.* introduced a method for the controlled fabrication of alloy electrodes with the desired phase to enhance product selectivity and long-term stability. They employed electrodeposition and thermal aging process to develop bimetallic HFGDEs with distinguished alloy phases (Fig. 16a). To achieve this, the electrodeposited Sn and Cu layers are converted into Cu_3Sn or Cu_6Sn_5 single phases, and the distinctive formation of these phases is controlled by monitoring Sn layer thickness and the aging duration. The resulting significant roughness and improved wettability of the alloy surface can be attributed to Cu/Sn atom transfer within the Sn layer and Cu substrate during aging and alloy formation. They achieved FE > 80% for formate production and a partial current density of 136 mA cm^{-2} with Cu_5Sn_6 HFGDE.[100]

As previously discussed, CO is used as a starting material to synthesize a wide range of basic chemicals, including ammonia, phosgene, and alcohol.[130] However, the more negative reduction potential required for CO production leads to the HER on the cathode. This can be mitigated using a highly efficient electrocatalyst with high intrinsic activity and selectivity for CO production or a suitable electrode configuration.[103] In this regard, Chen *et al.* developed a Cu HFGDE with a catalyst composed of hierarchical sub-nano AgZn bimetallic nanosheets, providing numerous active sites and enhancing charge transfer (Fig. 16b). The synergistic effect between Ag and Zn enhances the adsorption binding energy of COOH* intermediate, leading to reduced charge transfer resistance and fast eCO$_2$RR kinetics for CO formation. This has resulted in a high partial current density of 82.5 mA cm^{-2} and a high CO production rate of 1364.5 μmol h^{-1} cm^{-2} at applied potential −1.3 V *vs.* RHE.[103] Bimetallic interfaces on GDE surfaces represent an effective strategy for modulating eCO$_2$RR pathways. Applying this concept, Ma *et al.* developed bimetallic Cu–Bi microtubular electrodes with tunable interfaces for the efficient electroreduction of CO$_2$ to formate (Fig. 16c). Outperforming monometallic Cu HFGDEs, these bimetallic Cu/Bi HFGDEs demonstrated enhanced performance, including >90% FE for formate across a low potential window (−0.9 to −1.1 V *vs.* RHE), and an excellent formate partial current density more than five times higher. These favourable observations can be ascribed to the increased number of active sites and the lower charge transfer resistance.[172]

5.2.4 Halide modulation.

Halide ions optimize the electrical states and product distribution, and regulate the adsorption of key species, leading to enhanced eCO$_2$RR performances.[142] Halide ions can be incorporated either by adding them to the electrolyte, which enables specific adsorption on the electrode surface,[142] or through direct modification of the electrocatalyst with halide species.[173] Zhu *et al.* reported a halide-modulated hollow fiber Cu penetration electrode for efficient C$_{2+}$ production by eCO$_2$RR reaching ampere-level currents. The electrode exhibited notable C–C coupling capability by modulating the electronic states through halide ion coordinated adsorption. It demonstrated a FE of 68.8% at 2.1 A cm^{-2} in 3.0 M KI and remained stable during 120 h electrolysis at 2.0 A cm^{-2}. These superior performances are due to the combined effect of penetration effect and halide ion

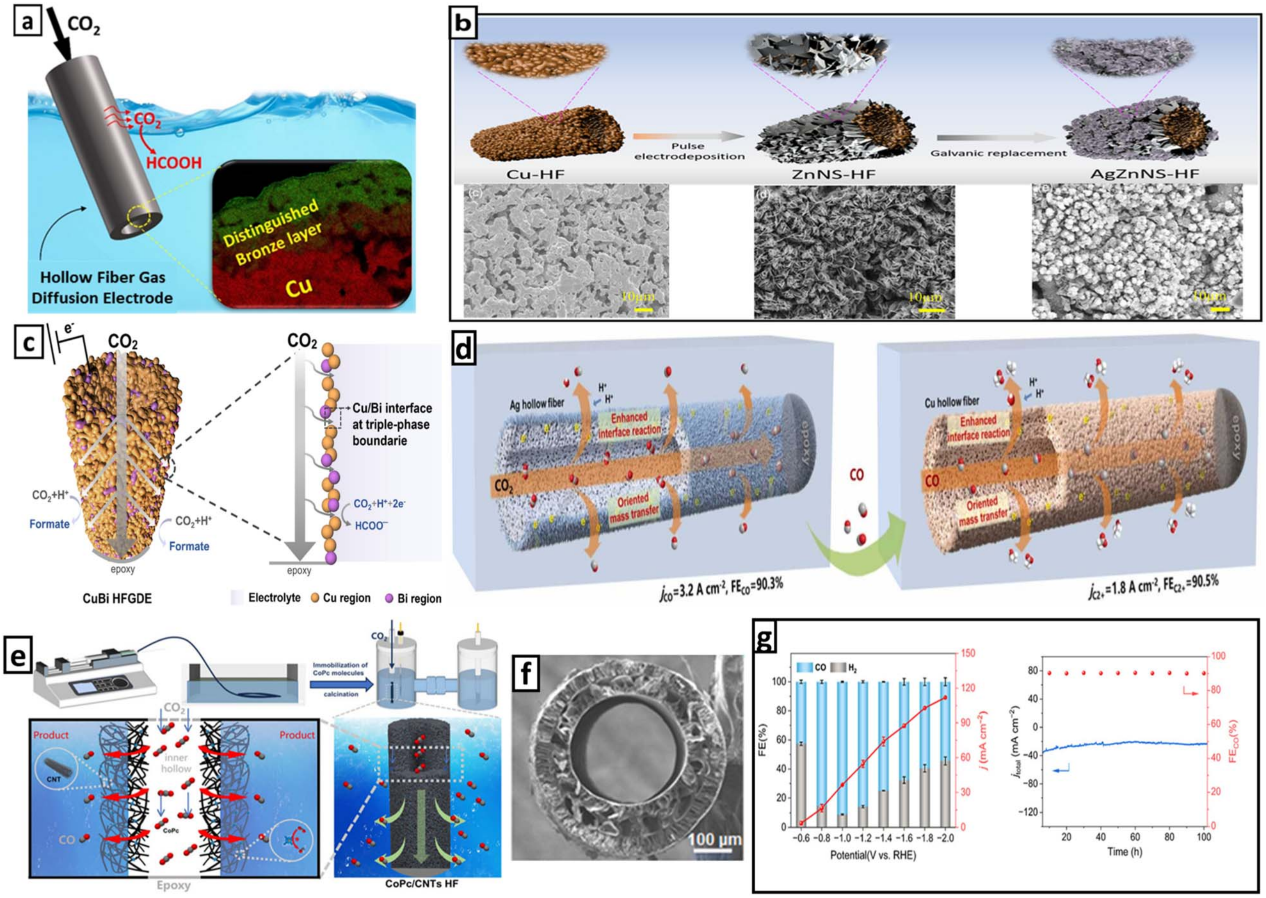

Fig. 16 (a) Bimetallic HFGDEs with distinguished alloy phases. Reproduced with permission.[100] Copyright 2021, Elsevier. (b) Schematic illustration of preparation of sub-nano AgZn bimetal nanosheets on Cu HFGDE (upper) and surface SEM images of Cu hollow fiber, Zn nanosheet hollow fiber and AgZn bimetal nanosheet hollow fiber, respectively, from left to right (below). Reproduced with permission.[103] Copyright 2024, Wiley-VCH Verlag GmbH & Co. KGaA, Weinheim. (c) Schematic illustration of bimetallic Cu–Bi microtubular electrode and formation of Cu/Bi interface at the triple-phase boundary. Reproduced with permission.[172] Copyright 2025, Elsevier. (d) Serially arranged Ag and Cu hollow-fiber penetration electrodes. Reproduced with permission.[150] Copyright 2023, Elsevier. (e) Schematic illustrations of CoPc catalyst immobilized carbon nanotube-interconnected hollow fiber. Reproduced with permission.[176] Copyright 2024, American Chemical Society. (f) SEM image of the cross-section of carbon HFGDEs modified with an unsaturated Ni–N_2 coordination structure. (g) Performance characteristics of carbon HFGDE with unsaturated Ni–N_2 coordination: FEs for CO and H_2 under various potentials (left) and long-term stability at a potential of −1.0 V *vs.* RHE (right). Reproduced with permission.[175] Copyright 2025, Wiley-VCH Verlag GmbH & Co. KGaA, Weinheim.

coordinated adsorption, which promotes the transfer of electrons to CO_2, reduces the C–C coupling energy, and suppresses proton adsorption, thereby reducing hydrogen evolution.[142]

Overcoming limitations such as low selectivity and undesired side reactions associated with direct CO_2 electroreduction into C_{2+} products, Dong *et al.* have utilized stepwise electroreductions of CO_2 to CO and then to C_{2+} products, presenting prospects for efficient eCO_2R for high-value C_{2+} chemicals.[150] They have developed a virtue of serial Ag and Cu hollow-fiber penetration electrodes (Fig. 16d), leading to highly efficient CO_2 electroreduction to C_{2+} products with a partial current density of 1.8 A cm^{-2} and a FE of 90.5%. These superior performances can be attributed to the synergetic combination of the unique penetration effect induced by hierarchical micro/nanostructured hollow fiber configurations and regulated electronic structures induced by chloride ion adsorption, which leads to favorable CO dimerization.[150] Wei *et al.* developed chlorine-doped SnO_2 nanoflowers on three-dimensional nickel hollow fibers to achieve superior electrocatalytic activity for the reduction of CO_2 to formate. They reported a CO_2 single-pass conversion rate of 93% at 2 A cm^{-2} and excellent stability, maintaining a formate selectivity above 94% for 520 h at a current density of 3 A cm^{-2}. These enhanced performances are attributed to the incorporation of chlorine into SnO_2, which promotes better electron transport and stronger CO_2 adsorption, thereby substantially lowering the energy barrier for *OCHO intermediate formation and enhancing formate generation.[174]

5.2.5 Carbon materials integration.

The development of carbon HFGDEs with efficient CO_2 electrocatalytic performance remains relatively underexplored and poses significant challenges. They hold great promise for eCO_2R due to their abundance, high stability, and easily tunable structures.[175] Further, to reduce the cost of mass production and improve the practical application at scale, scientists have focused on carbon-based hybrid gas-penetrable electrodes with integrated structures as an alternative to electrodes that use high-purity metals. In this regard, Zhang *et al.* have developed a carbon-based gas-penetrable electrode for the electrosynthesis of CO by immobilizing cobalt phthalocyanine (CoPc) molecular electrocatalyst on the surface of a carbon nanotube-interconnected hollow fiber (Fig. 16e). Here, enhanced CO_2 mass transfer and the abundance of well-defined triphasic reaction interfaces enable a maximum partial current density of 153.4 mA cm^{-2} at −0.93 V *vs.* RHE, achieving a peak FE of 96.5% and maintaining stable performance for at least 20 h.[176]

The incorporation of heteroatoms such as nitrogen (N), phosphorus (P), or sulfur (S) into carbon frameworks can modify the local electronic environment, converting inert carbon into active sites for CO_2 adsorption and conversion. In addition, carbon electrodes can effectively support single-metal atoms *via* nitrogen coordination, thereby increasing the density of active sites and improving catalytic performance. Therefore, to enhance the kinetics of CO_2 electroconversion to CO, Wang *et al.* developed carbon HFGDEs modified with an unsaturated Ni–N_2 coordination structure (Fig. 16f). In particular, the unsaturated Ni–N_2 coordination with symbiotic Ni_2 clusters significantly reduced the energy barrier for the formation of the key intermediate *COOH, achieving a FE of 91.0% and excellent stability for CO generation over 100 h at −1.0 V *versus* RHE (Fig. 16g).[175]

It can be witnessed that continued innovation in GDE design has resulted in a variety of structural modifications that enhance mass transport, improve electrochemical performance, ensure long-term operational stability, and ultimately support industrial-scale application. Fig. 17 depicts the different GDE architectures that have been developed over recent years, and Table 1 summarizes the key advancements in GDE architecture and associated performance outcomes.

According to Table 1, the highest performances have been achieved using HFGDEs, with maximum reported current densities reaching 3.2 A cm^{-2} for CO and 2.1 A cm^{-2} for C_{2+} products. Further, FE of up to 100% for CO and 90% for C_{2+} products have been reported. In terms of operational stability, the longest durations reported are 168 h for CO production, 520 h for formate production, and 120 h for C_{2+} product generation. Moreover, low potential values have been attained, with the lowest reported value being −0.45 V. It is important to

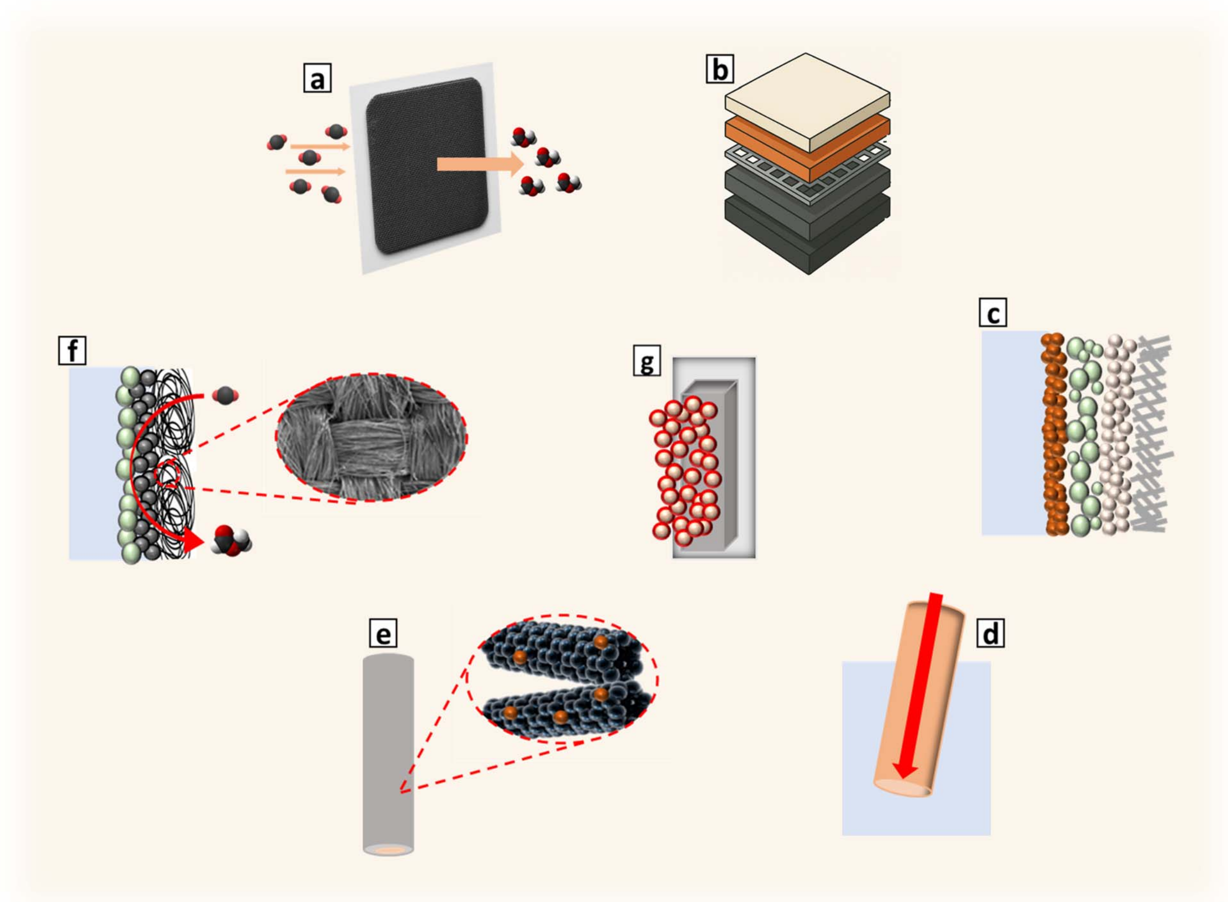

Fig. 17 GDEs with different architectures. (a) Mesh GDEs, (b) carbon-based asymmetrical hybrid GDEs, (c) heteroarchitectural GDEs, (d) self-supported HFGDEs, (e) carbon-based hybrid gas-penetrable electrodes, (f) woven GDEs, and (g) carbon-free GDEs.

Table 1 Summary of recent advancements in GDE structural and configurational modifications

Modification/study	Product	FE (%)	Current density (mA cm^{-2})	Stability (h)	Potential (V)	Remarks	Ref.
Zn nanosheets incorporated in B-doped Cu catalyst	C_{2+} products	78	−194	—	−0.45	- The incorporation of Zn nanosheets positively shifted the overpotential for *OCO formation	4
Optimizing the triple-phase interface by controlling the PTFE hydrophobic binder content and tuning the catalyst loading						- Mitigated flooding effect	
PTFE-modified Cu nanoparticles for the catalyst	C_{2+} products	78	−500	12	—	- Interconnected porous 3D micro-granule structure promoted the catalyst–electrode–CO_2 interfacial area and GDE hydrophobicity	106
Porous Cu–PTFE hybrid electrocatalyst	C_2H_4	51.1	−300	24	—	- Decreased FE for H_2 (11.6%)	110
Heteroatom (N, P, S, O) engineering on Cu catalyst	C_{2+} products	73.7	−1100	—	−1.15	- Suppressed HER energy efficiency	111
Study the polymer electrolyte membranes and optimization of total-catalyst-to-PTFE ionomer. Adding a thin liquid buffer layer between the cathode and the membrane – cathode feeding method	CO	—	−(122–247)	—	−2.0	- For high current efficiency, anion exchange membranes are suitable - 93.8% current efficiency and 68.7% energy efficiency - Mass activity for CO production of 613.5 A per g Au	112
Adding carbon support to the Au catalyst and studying the effect of membrane selection on catalyst performance	CO	<100	—	—	−0.7	- Anion exchange membranes yielded higher current densities than cation exchange membranes with the same catalyst	92
Electrolyte management through submillimeter cracks in the microporous layer	CO	—	−283	—	—	—	93
Carbon-based asymmetrical hybrid GDE (high porosity in the GDL and less porosity in the catalyst layer)	C_1 and C_2 products	70	Up to −200	—	−0.61	- Reduced HER - GDE structure with five components (PTFE layer, catalyst layer, Ni mesh, PEEK layer, and GDL)	38
Carbon cloth GDL	CO	69	−200	125	—	- Liquid overpressures of 100 mbar	62
Falling film design for electrolyte	CO	90	−100	—	5.5	- Electrolyte flow rate of 4000 mL min^{-1} - 100 cm^2 Ag GDE	31
Carbon-free GDEs (97 wt% Ag, 3 wt% PTFE)	CO	≤40	−200	<90 min	−1.8	- Electrowetting reduced the hydrophobicity of the porous GDE - Poor chemical stability	30
Mesh-GDL	C_2H_4	—	−500	100	—	- Flooding resistance without compromising conductivity	17
TiB_2–Ag–PTFE heteroarchitectural GDL	C_2H_4	64.7	−1200	>40	—	- Good conductivity - Strong hydrophobicity - High chemical stability - Compatibility with various catalysts and electrolytes	177

Table 1 (*Contd.*)

Modification/study	Product	FE (%)	Current density (mA cm^{-2})	Stability (h)	Potential (V)	Remarks	Ref.
Multifunctional metallic current collector design	CO, CH_4, C_2H_4	≤40	−700	—	2–6	- Targeting larger CO_2 electrolyzers for scale up processes while maintaining high FE	8
CO_2-phil microgels with pyridine-based amine moieties to tune the microenvironment of PTFE-based GDEs	C_2H_4	56	−700	—	−4	- Overcoming low CO_2 availability in the vicinity of the catalyst layer	20
Heterogeneous catalyst adlayer consisting of covalent organic framework nanoparticles and cation-exchange ionomers	C_{2+}	75	−200	—	—	- Multicarbon energy efficiency of 25%, suppresses hydrogen evolution and promotes CO_2-to-multicarbon product conversion in strong acid	147
Gas–liquid–solid interface modification	CO	≤92.1	>−100	10	−0.47	- PTFE modified carbon fiber paper as a superhydrophobic porous GDL (external water contact angle of 151 ± 2°) - Au NPs and carbon black catalyst maintained 80% of the initial CO_2 concentration at the interface	36
Utilization of CTAB as the electrolyte additive	CO	>90	—	—	—	- Modulated microenvironment at the electrode–electrolyte interface - Capable of operating in a wide potential range at high current densities	22
Robust and self-supported Cu flow-through GDEs	Formate	76	−265	—	−0.9	- Stable operation for several hours due to the combined phase inversion and calcination process of the Cu FTGDEs	159
Architecturally optimized Zn HFGDE	CO	90	−800	110	—	- Maintenance of metallic Zn^0 during eCO_2RR	160
Tubular Cu GDEs with modified pore network	CO, HCOOH, CH_4 and C_2H_4	CO < 20, other < 10	−100	—	−1.1	- Fabricated *via* selective laser melting	161
Tubular 3D printed Cu GDEs (solid, porous, and hybrid porous)	CO, HCOOH, CH_4 and C_2H_4	CO < 15 HCOOH < 10 Other ≤ 5	−500	—	—	- Study conducted at different flow regimes: flow-through and flow-by modes, shortened diffusion pathways	155
Cu HFGDE composed of metallic Cu with hierarchical pore structures	Formate	80	−210	1	—	- A robust self-supported GDE without any binder due to phase-inversion/sintering process - Formate yield of 2677 µmol h^{-1} cm^{-2}	152
Ag HFGDE composed of fused metallic Ag particles only	CO	>92	−150	100	—	- Unique pore structures - Tough self-supported GDE without any binder	99

Table 1 (*Contd.*)

Modification/study	Product	FE (%)	Current density (mA cm^{-2})	Stability (h)	Potential (V)	Remarks	Ref.
Application of 5 wt% PTFE water solution treatment to pristine 2D Zn nanosheets deposited Cu hollow fiber	CO	~83	−251.8	25	−1.1	- Decreased lumen side pressure - Enhanced CO_2 bubbling - CO product rate of 4696.9 μmol h^{-1} cm^{-2}	25
Porous Ag microparticle-based HFGDE	CO	94	−83.4	—	—	- A facile strategy for surface reconstruction of electrocatalysts	158
HFGDEs with Zn crystal facets controlled nanosheet catalysts	Syngas	>90	−73.3	—	−1.3	- Controlled modifications of surface free energy - Tuned Zn crystal growth orientation - High syngas production rate of 1328.6 μmol h^{-1} cm^{-2}	101
A layer of Cu nanocubes as the catalyst layer on HFGDEs (tuning the Cu catalyst shape morphology and promoting the oriented growth of nanocubes on the outer surface of HFGDEs)	C_{2+}	C_{2+} products (>90) Ethylene as the main product (>65)	>−470 for ethylene	36	−0.8 V	- Dominant Cu (100) facet in Cu nanocubes with high C_{2+} selectivity	97
HFGDE with hierarchical micro/nanostructures composed of metallic Ag	CO	~93	~−1260	168	−0.83	- >50% conversions through electrochemical redox treatment to rearrange the ordered nanorods on the surface	153
HFGDEs with *in situ* grown, defect-rich silver nanosheets	CO	93.5	−381.8	48	−0.8	- At low current densities: the catalyst activity primarily governs the reaction - At high current densities: the availability of CO_2 becomes the determining factor	170
Cu HFGDE with a Bi embedded carbon nanotube catalyst layer	Formate	>90	~−150	—	—	- Distinct wetting regions on a dual-layer HFGDE (distinctive hydrophilic–hydrophobic layers are created by *in situ* electrooxidation)	102
Bimetallic HFGDEs with distinguished alloy phases (stand-alone alloy HFGDEs)	Formate	>80	−136	—	−1.1	- Improved charge transfer and surface wettability	100
Cu HFGDE with a catalyst composed of hierarchical sub-nano AgZn bimetallic nanosheets	CO	>83	−82.5	24	−1.3	- High CO production rate of 1364.5 μmol h^{-1} cm^{-2} - Charge transfer resistance of 4.4 Ω, confirming a fast electron transfer and improved kinetics in GDE mode	103
Bimetallic Cu–Bi microtubular electrodes	Formate	>90	−115	16	−0.9 to −1.1	- Bimetallic interfaces at triple-phase boundaries	172
Halide-modulated hollow fiber Cu penetration electrode	C_{2+}	68.8	−2100	120	—	- Penetration effect and halide ion coordinated adsorption - The modulated electronic structures by halide ion adsorption facilitated the C–C coupling of intermediates	142

Table 1 (*Contd.*)

Modification/study	Product	FE (%)	Current density (mA cm^{-2})	Stability (h)	Potential (V)	Remarks	Ref.
Serial Ag and Cu hollow-fiber penetration electrodes	CO and C_{2+}	CO (90.3) C_{2+} (90.5)	$CO_2 \rightarrow CO$ (−3200) $CO \rightarrow C_{2+}$ (−1800)	—	—	- Regulated electronic structures induced by Cl ion adsorption (CO dimerization from Cl^- regulated electronic structures)	150
Chlorine-doped SnO_2 nanoflowers on nickel HFGDE	Formate	>94	−3000	520	—	- CO_2 single-pass conversion rate of 93% at 2 A cm^{-2}	174
Immobilization of the CoPc molecular electrocatalyst on the surface of a carbon nanotube interconnected hollow fiber	CO	96.5	−153.4	20	−0.93	- Carbon-based hybrid GPEs with integrated structure and high performance	176
Carbon HFGDEs modified with an unsaturated Ni–N_2 coordination structure	CO	91	−61	100	−1.0	- Ni–N_2 structure lowers the energy barriers for COOH* intermediate formation	175

consider that when engineering GDEs with a focus on improving a specific characteristic, any new structural adjustments or material changes can also impact other performance metrics. Therefore, it is crucial to establish a balance and maintain key performance parameters at optimum levels simultaneously for proper functioning.

6. Conclusions and future perspectives

In recent years, researchers have put considerable effort into optimizing the structure and composition of GDEs to achieve durable, efficient and selective eCO_2R. They have concentrated their efforts particularly on improving the GDLs, catalyst layers, membranes, electrolytes, and interfaces within GDEs. Focusing on these key components, they have tackled various issues such as flooding, perspiration, salt precipitation, low selectivity, poor stability, high overpotential, H_2 evolution, cathodic corrosion, high cell resistance, *etc.* Significant progress in overcoming these challenges has been made by carefully choosing appropriate materials and employing rational design principles to optimize each component and its integration within the system. Advancements have been made in engineering different components of GDEs and in configurational changes. Particularly, GDE configuration has been transitioned from conventional planar GDEs to HFGDEs and various improved versions of planar GDEs, including woven, heteroarchitectural, and carbon-free, can be identified. These advancements have led to achieving ampere-level current densities, high FE values, low potentials and enhanced stability exceeding 100 h. However, despite significant advances in the last few years, there are multiple opportunities for further improvement. Particularly, to enable scalable production, while factors such as selectivity and efficiency are crucial, special attention should also be paid to achieve stable operation for tens of thousands of hours, which would be a practical requirement. None of the reported experimental works demonstrated stability more than 1000 h. Further, eCO_2R should be more focused on C_{2+} product formation, which is relatively low compared to CO and formate like C_1 products. Future research should specifically focus on improving the FE for multi-carbon product formation. Therefore, further progress in both experimental and theoretical domains is essential to achieve a comprehensive understanding of the CO_2 reduction process. A thorough understanding of the mechanisms involved in the formation of highly reduced products is still required, including the influence of various factors such as potential, pH, and gas pressure on different reaction pathways.

Catalyst advancements have taken place, including altering the oxidation state, morphology, and exposed facets of catalysts; utilizing bimetallic alloys; heteroatom engineering; employing sacrificial anodes and pore builders; using carbon supports for catalyst nanoparticles; developing hydrophobic catalysts; and polymer modifications. Further, experimental investigations are necessary to identify the surface reaction mechanisms, surface reconstruction during eCO_2R, and true active sites on catalyst surfaces that exhibit complex, multifaceted structural features. Achieving a well-balanced interaction of intermediates with the catalyst surface, and an adequate residence time on active sites is crucial for certain rate-determining steps in the formation of highly reduced products. This is critical for assessing catalyst activity and reaction rates, which are essential in industrial relevance. Advanced spectroscopic techniques, including attenuated total reflection-infrared, surface-enhanced Raman spectroscopy, X-ray absorption spectroscopy alongside with computational methods, are crucial for elucidating reaction mechanisms. Further, engineering two-dimensional (2D) materials such as transition metal carbides and nitrides (MXenes), 2D metal-organic frameworks (MOFs), and covalent organic frameworks (COFs) can be suggested as catalyst materials. Activity and selectivity of the catalyst can be highly enhanced by regulating electronic structure and active sites through atomic-level engineering strategies. Operating eCO_2R at commercially relevant reaction rates (current densities $\geq$ 200 mA cm^{-2} and FE $\geq$ 95%) demands efficient and stable catalysts and facile mass transport of reactants and products, with minimized energy losses.

GDL is a crucial component within GDEs and has undergone immense changes to improve mass diffusion and avoid flooding and salt accumulation. Variations in GDL structure, such as different porosities and microporous layers with different crack abundances, as well as PTFE-based superhydrophobic porous GDLs (carbon-free GDLs) have been reported within the past few years. To move the eCO_2R technology forward, next-generation GDLs capable of maintaining stable performance at high current densities are required. GDLs made from electrospun carbon nanofibers and aerogels can be suggested as good solutions for achieving tunable and ultrahigh porosity, respectively. Even though carbon-free superhydrophobic GDLs have taken improved attention as a viable solution for flooding issues, their non-conductive nature and the associated challenges in current collection have long been understudied, imposing limitations on industrial scale-up unless viable solutions for current collection are developed. It should be focused on uniform applied potential in the catalyst layer and current distribution to achieve long-term stability and product selectivity. Investigations into new current collector designs are required for large-scale systems. Therefore, further exploration into incorporating metallic networks to enhance electrical conductivity and employing non-invasive current collectors to improve current collection and distribution in non-conductive GDLs is suggested. In addition, enhancing C_{2+} product selectivity by directing the pathway toward thin-layer catalysts on ultra-hydrophobic GDEs would be a promising system to investigate.

Recently, the focus has shifted towards investigating interface engineering methods, surpassing efforts in structural design of GDEs. Advancements like achieving efficient conversion of CO_2 at ampere-level current densities have been enabled by adjusting the electrocatalytic microenvironment through three-phase interface engineering. Heterogeneous catalyst adlayers, creation of distinct wetting regions, surface modification at the electrode–electrolyte interface, and tuning microenvironment by adding CO_2-phil microgels to the catalyst layer can be identified as recent modifications. Moreover, gradient wettability designs and further exploration of surface chemistry modifications using CO_2-philic compounds are recommended. Optimizing electrolyte composition has also been utilized as an effective strategy. Recent studies have reported the incorporation of surfactant additives and halide ions into electrolyte solutions. For further improvements, developing electrolytes with tunable buffering capacities to sustain pH stability at high current densities can be suggested.

HFGDEs offer favorable prospects with significant performance improvements, even though they still deliver limited selectivities and stabilities for large-scale adoption. However, HFGDEs are the most effective configuration reported so far for eCO_2R due to superior gas accessibility near the catalytic sites facilitated by continuously delivering convective gas flow, thereby achieving abundant triple-phase interfaces and enhanced reaction kinetics. Recent studies utilizing HFGDEs reported ampere-level current densities for C_{2+} product formation in liquid electrolytes. Porous metallic HFGDEs represent a versatile and scalable electrode architecture for eCO_2R, and its optimization for industry-scale applications remains an active area of research. Future research efforts should particularly consider possible modifications to the microstructure and microenvironment, as well as improvements in stability. Uniform pore size distribution is required to enhance gas flow. To achieve this, it is suggested to utilize appropriate materials (*e.g.*, metal powder, binders) in the correct ratios and adjust process conditions (*e.g.*, temperature, duration). To avoid the flooding-related stability issues, adding hydrophobic compounds can be recommended. Another problem that significantly affects long-term stability is catalyst degradation or reduced activity, and more explorations are needed in terms of materials and fabrication. Moreover, investigations should focus specifically on hollow fiber arrays, fiber density, and arrangement.

The rational design of GDEs, including their compositions, morphologies, and structures, requires a comprehensive understanding of the structure–performance relationship. Further, the focus should be on fabricating cost-effective and lightweight GDEs while maintaining expected performance outcomes. The industrial applications of GDEs and the market can be expected to undergo substantial growth in the coming years. This growth is driven by the rising demand for sustainable commodity chemical production and clean energy sources, as well as increased investments in research and development activities in this area. We anticipate that continued and coordinated research efforts will pave the way towards the sustainable and large-scale production of many of our essential fuels and chemicals.

Conflicts of interest

There are no conflicts of interest to declare.

Data availability

No primary research results, software or code have been included and no new data were generated or analysed as part of this review.

Acknowledgements

The authors extend their sincere appreciation to all dedicated researchers in the Department of Chemistry at the University of Colombo, Sri Lanka, and to the global community of scientists who have made invaluable contributions towards advancing sustainable electrochemical technologies.

References

1 T. Sakakura, J. C. Choi and H. Yasuda, *Chem. Rev.*, 2007, **107**, 2365–2387.
2 Q. Liu, L. Wu, R. Jackstell and M. Beller, *Nat. Commun.*, 2015, **6**, 5933.
3 X. Huang, Q. Shen, J. Liu, N. Yang and G. Zhao, *Energy Environ. Sci.*, 2016, **9**, 3161–3171.
4 Y. Song, J. R. C. Junqueira, N. Sikdar, D. Öhl, S. Dieckhöfer, T. Quast, S. Seisel, J. Masa, C. Andronescu and W. Schuhmann, *Angew. Chem., Int. Ed.*, 2021, **60**, 9135–9141.
5 Q. W. Song, Z. H. Zhou and L. N. He, *Green Chem.*, 2017, **19**, 3707–3728.
6 P. Gao, S. Li, X. Bu, S. Dang, Z. Liu, H. Wang, L. Zhong, M. Qiu, C. Yang, J. Cai, W. Wei and Y. Sun, *Nat. Chem.*, 2017, **9**, 1019–1024.
7 W. A. Smith, T. Burdyny, D. A. Vermaas and H. Geerlings, *Joule*, 2019, **3**, 1822–1834.
8 M. Filippi, T. Möller, R. Pastusiak, E. Magori, B. Paul and P. Strasser, *ACS Energy Lett.*, 2024, **9**, 1361–1368.
9 X. Li, P. Anderson, H. R. M. Jhong, M. Paster, J. F. Stubbins and P. J. A. Kenis, *Energy Fuels*, 2016, **30**, 5980–5989.
10 Y. Hori, K. Kikuchi and S. Suzuki, *Chem. Lett.*, 2006, **14**, 1695–1698.
11 O. S. Bushuyev, P. De Luna, C. T. Dinh, L. Tao, G. Saur, J. van de Lagemaat, S. O. Kelley and E. H. Sargent, *Joule*, 2018, **2**, 825–832.
12 A. Otto, T. Grube, S. Schiebahn and D. Stolten, *Energy Environ. Sci.*, 2015, **8**, 3283–3297.
13 C. Chen, X. Sun, L. Lu, D. Yang, J. Ma, Q. Zhu, Q. Qian and B. Han, *Green Chem.*, 2018, **20**, 4579–4583.
14 L. Fan, C. Xia, F. Yang, J. Wang, H. Wang and Y. Lu, *Sci. Adv.*, 2020, **6**, eaay3111.
15 X. Zhang, S. X. Guo, K. A. Gandionco, A. M. Bond and J. Zhang, *Mater. Today Adv.*, 2020, **7**, 100074.
16 T. N. Nguyen and C. T. Dinh, *Chem. Soc. Rev.*, 2020, **49**, 7488–7504.
17 A. H. M. da Silva, S. J. Raaijman and P. J. Corbett, *Chem. Eng. J.*, 2024, **494**, 153266.
18 Z. Weng, Y. Wu, M. Wang, J. Jiang, K. Yang, S. Huo, X. F. Wang, Q. Ma, G. W. Brudvig, V. S. Batista, Y. Liang, Z. Feng and H. Wang, *Nat. Commun.*, 2018, **9**, 415.
19 D. Raciti and C. Wang, *ACS Energy Lett.*, 2018, **3**, 1545–1556.
20 H. Rabiee, M. Li, P. Yan, Y. Wu, X. Zhang, F. Dorosti, X. Zhang, B. Ma, S. Hu, H. Wang, Z. Zhu and L. Ge, *Adv. Sci.*, 2024, **11**, 2402964.
21 T. Burdyny and W. A. Smith, *Energy Environ. Sci.*, 2019, **12**, 1442–1453.
22 Y. Kuang, G. Chen, D. H. Mudiyanselage, H. Rabiee, B. Ma, F. Dorosti, A. K. Nanjundan, Z. Zhu, H. Wang and L. Ge, *Chem.–Eur. J.*, 2024, **30**, e202403251.
23 F. P. G. de Arquer, C. T. Dinh, A. Ozden, J. Wicks, C. McCallum, A. R. Kirmani, D. H. Nam, C. Gabardo, A. Seifitokaldani, X. Wang, Y. C. Li, F. Li, J. Edwards, L. J. Richter, S. J. Thorpe, D. Sinton and E. H. Sargent, *Science*, 2020, **367**, 661–666.
24 M. B. Ross, P. De Luna, Y. Li, C. T. Dinh, D. Kim, P. Yang and E. H. Sargent, *Nat. Catal.*, 2019, **2**, 648–658.
25 G. Chen, L. Ge, B. Ma, Y. Kuang, H. Rabiee, F. Dorosti, A. K. Nanjundan, Z. Zhu and H. Wang, *Appl. Catal. B Environ. Energy*, 2025, **363**, 124803.
26 H. Rabiee, B. Ma, Y. Yang, F. Li, P. Yan, Y. Wu, X. Zhang, S. Hu, H. Wang, L. Ge and Z. Zhu, *Adv. Funct. Mater.*, 2024, **35**, 2411195.
27 E. W. Lees, B. A. W. Mowbray, F. G. L. Parlane and C. P. Berlinguette, *Nat. Rev. Mater.*, 2022, **7**, 55–64.
28 I. E. L. Stephens, K. Chan, A. Bagger, S. W. Boettcher, J. Bonin, E. Boutin, A. K. Buckley, R. Buonsanti, E. R. Cave and X. Chang, *JPhys Energy*, 2022, **4**, 042003.
29 H. R. M. Jhong, S. Ma and P. J. Kenis, *Curr. Opin. Chem. Eng.*, 2013, **2**, 191–199.
30 L. M. Baumgartner, A. Goryachev, C. I. Koopman, D. Franzen, B. Ellendorff, T. Turek and D. A. Vermaas, *Energy Adv.*, 2023, **2**, 1893–1904.
31 M. Großeheide, D. Schaffeld, R. Keller and M. Wessling, *Electrochem. Commun.*, 2023, **150**, 107487.
32 Z. Kou, X. Li, T. Wang, Y. Ma, W. Zang, G. Nie and J. Wang, *Electrochem. Energy Rev.*, 2022, **5**, 82–111.
33 S. Matsuoka, T. Kohzuki, C. Pac, A. Ishida, S. Takamuku, M. Kusaba, N. Nakashima and S. Yanagida, *J. Phys. Chem.*, 1992, **96**, 4437–4442.
34 S. Xu and E. A. Carter, *Chem. Rev.*, 2019, **119**, 6631–6669.
35 D. M. Feng, Y. P. Zhu, P. Chen and T. Y. Ma, *Catalysts*, 2017, **7**, 373.
36 R. Shi, J. Guo, X. Zhang, G. I. N. Waterhouse, Z. Han, Y. Zhao, L. Shang, C. Zhou, L. Jiang and T. Zhang, *Nat. Commun.*, 2020, **11**, 3028.
37 M. R. Singh, E. L. Clark and A. T. Bell, *Phys. Chem. Chem. Phys.*, 2015, **17**, 18924–18936.
38 X. Wang, C. Tomon, T. Bobrowski, P. Wilde, J. R. C. Junqueira, T. Quast, W. He, N. Sikdar, J. Weidner and W. Schuhmann, *ChemElectroChem*, 2022, **9**, e202200675.
39 Z. Xing, L. Hu, D. S. Ripatti, X. Hu and X. Feng, *Nat. Commun.*, 2021, **12**, 136.
40 C. W. Li, J. Ciston and M. W. Kanan, *Nature*, 2014, **508**, 504–507.
41 B. Endrődi, G. Bencsik, F. Darvas, R. Jones, K. Rajeshwar and C. Janáky, *Prog. Energy Combust. Sci.*, 2017, **62**, 133–154.
42 K. Yang, R. Kas and W. A. Smith, *J. Am. Chem. Soc.*, 2019, **141**, 15891–15900.
43 S. Hernandez-Aldave and E. Andreoli, *Catalysts*, 2020, **10**, 713.
44 H. Ooka, M. C. Figueiredo and M. T. M. Koper, *Langmuir*, 2017, **33**, 9307–9313.

45 T. J. F. Day, U. W. Schmitt and G. A. Voth, *J. Am. Chem. Soc.*, 2000, **122**, 12027–12028.

46 B. M. Tackett, E. Gomez and J. G. Chen, *Nat. Catal.*, 2019, **2**, 381–386.

47 B. A. Rosen, A. Salehi-Khojin, M. R. Thorson, W. Zhu, D. T. Whipple, P. J. A. Kenis and R. I. Masel, *Science*, 2011, **334**, 643–644.

48 C. T. Dinh, T. Burdyny, M. G. Kibria, A. Seifitokaldani, C. M. Gabardo, F. P. G. de Arquer, A. Kiani, J. P. Edwards, P. D. Luna, O. S. Bushuyev, C. Zou, R. Q. Bermudez, Y. Pang, D. Sinton and E. H. Sargent, *Science*, 2018, **360**, 783–787.

49 M. R. Singh, Y. Kwon, Y. Lum, J. W. Ager and A. T. Bell, *J. Am. Chem. Soc.*, 2016, **138**, 13006–13012.

50 A. Wuttig, M. Yaguchi, K. Motobayashi, M. Osawa and Y. Surendranath, *Proc. Natl. Acad. Sci. U. S. A.*, 2016, **113**, E4585–E4593.

51 C. W. Lee, N. H. Cho, K. D. Yang and K. T. Nam, *ChemElectroChem*, 2017, **4**, 2130–2136.

52 J. T. Feaster, C. Shi, E. R. Cave, T. Hatsukade, D. N. Abram, C. H. Kendra, P. Kuhl, J. K. Nørskov and T. F. Jaramillo, *ACS Catal.*, 2017, **7**, 4822–4827.

53 J. Durst, A. Rudnev, A. Dutta, Y. Fu, J. Herranz, V. Kaliginedi, A. Kuzume, A. A. Permyakova, Y. Paratcha, P. Broekmann and T. J. Schmidt, *Chimia*, 2015, **69**, 769–776.

54 M. Jouny, W. Luc and F. Jiao, *Nat. Catal.*, 2018, **1**, 748–755.

55 J. Li, G. Chen, Y. Zhu, Z. Liang, A. Pei, C. L. Wu, H. Wang, H. R. Lee, K. Liu, S. Chu and Y. Cui, *Nat. Catal.*, 2018, **1**, 592–600.

56 D. M. Weekes, D. A. Salvatore, A. Reyes, A. Huang and C. P. Berlinguette, *Acc. Chem. Res.*, 2018, **51**, 910–918.

57 T. Zheng, K. Jiang, N. Ta, Y. Hu, J. Zeng, J. Liu and H. Wang, *Joule*, 2019, **3**, 265–278.

58 J. J. Carroll, J. D. Slupsky and A. E. Mather, *J. Phys. Chem. Ref. Data*, 1991, **20**, 1201–1209.

59 S. Verma, Y. Hamasaki, C. Kim, W. Huang, S. Lu, H. R. M. Jhong, A. A. Gewirth, T. Fujigaya, N. Nakashima and P. J. A. Kenis, *ACS Energy Lett.*, 2018, **3**, 193–198.

60 B. Kim, S. Ma, H. R. M. Jhong and P. J. A. Kenis, *Electrochim. Acta*, 2015, **166**, 271–276.

61 H. Yang, Q. Lin, C. Zhang, X. Yu, Z. Cheng, G. Li, Q. Hu, X. Ren, Q. Zhang, J. Liu and C. He, *Nat. Commun.*, 2020, **11**, 593.

62 L. M. Baumgartner, C. I. Koopman, A. Forner-Cuenca and D. A. Vermaas, *ACS Appl. Energy Mater.*, 2022, **5**, 15125–15135.

63 R. B. Kutz, Q. Chen, H. Yang, S. D. Sajjad, Z. Liu and I. R. Masel, *Energy Technol.*, 2017, **5**, 929–936.

64 D. A. Salvatore, D. M. Weekes, J. He, K. E. Dettelbach, Y. C. Li, T. E. Mallouk and C. P. Berlinguette, *ACS Energy Lett.*, 2018, **3**, 149–154.

65 S. Verma, X. Lu, S. Ma, R. I. Masel and P. J. A. Kenis, *Phys. Chem. Chem. Phys.*, 2016, **18**, 7075–7084.

66 Y. Chen, A. Vise, W. E. Klein, F. C. Cetinbas, D. J. Myers, W. A. Smith, T. G. Deutsch and K. C. Neyerlin, *ACS Energy Lett.*, 2020, **5**, 1825–1833.

67 C. Pan, Q. Li, J. O. Jensen, R. He, L. N. Cleemann, M. S. Nilsson, N. J. Bjerrum and Q. Zeng, *J. Power Sources*, 2007, **172**, 278–286.

68 V. K. Mathur and J. Crawford, *Recent Trends in Fuel Cell Science and Technology*, 2007, vol. 400, pp. 116–128.

69 S. Ma, M. Sadakiyo, R. Luo, M. Heima, M. Yamauchi and P. J. A. Kenis, *J. Power Sources*, 2016, **301**, 219–228.

70 N. T. Nesbitt, T. Burdyny, H. Simonson, D. Salvatore, D. Bohra, R. Kas and W. A. Smith, *ACS Catal.*, 2020, **10**, 14093–14106.

71 N. Furuya, T. Yamazaki and M. Shibata, *J. Electroanal. Chem.*, 1997, **431**, 39–41.

72 A. Forner-Cuenca, J. Biesdorf, L. Gubler, P. M. Kristiansen, T. J. Schmidt and P. Boillat, *Adv. Mater.*, 2015, **27**, 6317–6322.

73 B. Kim, F. Hillman, M. Ariyoshi, S. Fujikawa and P. J. A. Kenis, *J. Power Sources*, 2016, **312**, 192–198.

74 A. Z. Weber and J. Newman, *J. Electrochem. Soc.*, 2005, **152**, A677.

75 G. L. De Gregorio, T. Burdyny, A. Loiudice, P. Iyengar, W. A. Smith and R. Buonsanti, *ACS Catal.*, 2020, **10**, 4854–4862.

76 K. Yang, R. Kas, W. A. Smith and T. Burdyny, *ACS Energy Lett.*, 2021, **6**, 33–40.

77 X. She, T. Zhang, Z. Li, H. Li, H. Xu and J. Wu, *Cell Rep. Phys. Sci.*, 2020, **1**, 100051.

78 W. Ma, S. Xie, T. Liu, Q. Fan, J. Ye, F. Sun, Z. Jiang, Q. Zhang, J. Cheng and Y. Wang, *Nat. Catal.*, 2020, **3**, 478–487.

79 Q. Wang, H. Dong, H. Yu and H. Yu, *J. Power Sources*, 2015, **279**, 1–5.

80 H. B. Yang, S. F. Hung, S. Liu, K. Yuan, S. Miao, L. Zhang, X. Huang, H. Y. Wang, W. Cai, R. Chen, J. Gao, X. Yang, W. Chen, Y. Huang, H. M. Chen, C. M. Li, T. Zhang and B. Liu, *Nat. Energy*, 2018, **3**, 140–147.

81 Y. Zhou, F. Che, M. Liu, C. Zou, Z. Liang, P. De Luna, H. Yuan, J. Li, Z. Wang, H. Xie, H. Li, P. Chen, E. Bladt, R. Quintero-Bermudez, T. K. Sham, S. Bals, J. Hofkens, D. Sinton, G. Chen and E. H. Sargent, *Nat. Chem.*, 2018, **10**, 974–980.

82 M. Liu, Y. Pang, B. Zhang, P. De Luna, O. Voznyy, J. Xu, X. Zheng, C. T. Dinh, F. Fan, C. Cao, F. P. G. de Arquer, T. S. Safaei, A. Mepham, A. Klinkova, E. Kumacheva, T. Filleter, D. Sinton, S. O. Kelley and E. H. Sargent, *Nature*, 2016, **537**, 382–386.

83 S. Popović, M. Smiljanić, P. Jovanovič, J. Vavra, R. Buonsanti and N. Hodnik, *Angew. Chem., Int. Ed.*, 2020, **59**, 14736–14746.

84 R. S. Kanase, M. Arunachalam, J. Badiger, S. A. Sayed, K. S. Ahn and S. H. Kang, *Int. J. Hydrogen Energy*, 2025, **124**, 370–385.

85 A. Vasileff, C. Xu, Y. Jiao, Y. Zheng and S. Z. Qiao, *Chem*, 2018, **4**, 1809–1831.

86 C. W. Lee, K. D. Yang, D. H. Nam, J. H. Jang, N. H. Cho, S. W. Im and K. T. Nam, *Adv. Mater.*, 2018, **30**, 1704717.

87 S. Lee, D. Kim and J. Lee, *Angew. Chem., Int. Ed.*, 2015, **54**, 14701–14705.

88 S. Nitopi, E. Bertheussen, S. B. Scott, X. Liu, A. K. Engstfeld, S. Horch, B. Seger, I. E. L. Stephens, K. Chan, C. Hahn, J. K. Nørskov, T. F. Jaramillo and I. Chorkendorff, *Chem. Rev.*, 2019, **119**, 7610–7672.

89 C. Chen, J. F. K. Kotyk and S. W. Sheehan, *Chem*, 2018, **4**, 2571–2586.
90 Z. Yin, C. Yu, Z. Zhao, X. Guo, M. Shen, N. Li, M. Muzzio, J. Li, H. Liu, H. Lin, J. Yin, G. Lu, D. Su and S. Sun, *Nano Lett.*, 2019, **19**, 8658–8663.
91 Z. Q. Liang, T. T. Zhuang, A. Seifitokaldani, J. Li, C. W. Huang, C. S. Tan, Y. Li, P. De Luna, C. T. Dinh, Y. Hu, Q. Xiao, P. L. Hsieh, Y. Wang, F. Li, R. Q. Bermudez, Y. Zhou, P. Chen, Y. Pang, S. C. Lo, L. J. Chen, H. Tan, Z. Xu, S. Zhao, D. Sinton and E. H. Sargent, *Nat. Commun.*, 2018, **9**, 3828.
92 S. Alinejad, J. Quinson, Y. Li, Y. Kong, S. Reichenberger, S. Barcikowski, P. Broekmann and M. Arenz, *J. Catal.*, 2024, **429**, 115209.
93 Y. Kong, M. Liu, H. Hu, Y. Hou, S. Vesztergom, M. d. J. Gálvez-Vázquez, I. Z. Montiel, V. Kolivoška and P. Broekmann, *Small Methods*, 2022, **6**, 2200369.
94 J. Lee, J. Lim, C. W. Roh, H. S. Whang and H. Lee, *J. CO2 Util.*, 2019, **31**, 244–250.
95 L. C. Weng, A. T. Bell and A. Z. Weber, *Energy Environ. Sci.*, 2019, **12**, 1950–1968.
96 A. Angulo, P. van der Linde, H. Gardeniers, M. Modestino and D. F. Rivas, *Joule*, 2020, **4**, 555–579.
97 H. Rabiee, J. K. Heffernan, L. Ge, X. Zhang, P. Yan, E. Marcellin, S. Hu, Z. Zhu, H. Wang and Z. Yuan, *Appl. Catal., B*, 2023, **330**, 122589.
98 H. Rabiee, X. Zhang, L. Ge, S. Hu, M. Li, S. Smart, Z. Zhu and Z. Yuan, *ACS Appl. Mater. Interfaces*, 2020, **12**, 21670–21681.
99 S. Li, X. Dong, W. Chen, Y. Song, G. Li, W. Wei and Y. Sun, *Catalysts*, 2022, **12**, 453.
100 H. Rabiee, L. Ge, X. Zhang, S. Hu, M. Li, S. Smart, Z. Zhu, H. Wang and Z. Yuan, *Appl. Catal., B*, 2021, **298**, 120538.
101 G. Chen, L. Ge, Y. Kuang, H. Rabiee, B. Ma, F. Dorosti, A. K. Nanjundan, Z. Zhu and H. Wang, *Chem. Eng. J.*, 2024, **490**, 151651.
102 H. Rabiee, L. Ge, J. Zhao, X. Zhang, M. Li, S. Hu, S. Smart, T. E. Rufford, Z. Zhu, H. Wang and Z. Yuan, *Appl. Catal., B*, 2022, **310**, 121362.
103 G. Chen, L. Ge, Y. Kuang, H. Rabiee, B. Ma, F. Dorosti, A. K. Nanjundan, Z. Zhu and H. Wang, *Small Sci.*, 2024, **4**, 2400184.
104 D. Wang, J. Mao, C. Zhang, J. Zhang, J. Li, Y. Zhang and Y. Zhu, *eScience*, 2023, **3**, 100119.
105 Y. Y. Birdja, E. Pérez-Gallent, M. C. Figueiredo, A. J. Göttle, F. Calle-Vallejo and M. T. M. Koper, *Nat. Energy*, 2019, **4**, 732–745.
106 J. Pellessier, X. Gong, B. Li, J. Zhang, Y. Gang, K. Hambleton, C. Podder, Z. Gao, H. Zhou, G. Wang, H. Pan and Y. Li, *J. Mater. Chem. A*, 2023, **11**, 26252–26264.
107 F. Pan, B. Li, W. Deng, Z. Du, Y. Gang, G. Wang and Y. Li, *Appl. Catal., B*, 2019, **252**, 240–249.
108 X. Chen, J. Chen, N. M. Alghoraibi, D. A. Henckel, R. Zhang, U. O. Nwabara, K. E. Madsen, P. J. A. Kenis, S. C. Zimmerman and A. A. Gewirth, *Nat. Catal.*, 2021, **4**, 20–27.
109 X. Wei, Z. Yin, K. Lyu, Z. Li, J. Gong, G. Wang, L. Xiao, J. Lu and L. Zhuang, *ACS Catal.*, 2020, **10**, 4103–4111.
110 Y. Seki, M. Nakabayashi, M. Sugiyama and T. Minegishi, *ChemElectroChem*, 2025, **12**, e202400536.
111 M. Zheng, P. Wang, X. Zhi, K. Yang, Y. Jiao, J. Duan, Y. Zheng and S. Z. Qiao, *J. Am. Chem. Soc.*, 2022, **144**, 14936–14944.
112 Y. Gu, J. Wei, X. Wu and X. Liu, *Sci. Rep.*, 2021, **11**, 11136.
113 D. Raciti, T. Braun, B. M. Tackett, H. Xu, M. Cruz, B. J. Wiley and T. P. Moffat, *ACS Catal.*, 2021, **11**, 11945–11959.
114 W. H. Lee, Y. J. Ko, Y. Choi, S. Y. Lee, C. H. Choi, Y. J. Hwang, B. K. Min, P. Strasser and H. S. Oh, *Nano Energy*, 2020, **76**, 105030.
115 C. M. Gabardo, C. P. O'Brien, J. P. Edwards, C. McCallum, Y. Xu, C. T. Dinh, J. Li, E. H. Sargent and D. Sinton, *Joule*, 2019, **3**, 2777–2791.
116 M. Maja, C. Orecchia, M. Strano, P. Tosco and M. Vanni, *Electrochim. Acta*, 2000, **46**, 423–432.
117 Z. Xing, X. Hu and X. Feng, *ACS Energy Lett.*, 2021, **6**, 1694–1702.
118 K. Liu, W. A. Smith and T. Burdyny, *ACS Energy Lett.*, 2019, **4**, 639–643.
119 K. J. Puring, D. Siegmund, J. Timm, F. Möllenbruck, S. Schemme, R. Marschall and U. P. Apfel, *Adv. Sustainable Syst.*, 2021, **5**, 2000088.
120 T. Burchardt, *J. Power Sources*, 2004, **135**, 192–197.
121 D. G. Wheeler, B. A. W. Mowbray, A. Reyes, F. Habibzadeh, J. He and C. P. Berlinguette, *Energy Environ. Sci.*, 2020, **13**, 5126–5134.
122 M. E. Leonard, M. J. Orella, N. Aiello, Y. Román-Leshkov, A. Forner-Cuenca and F. R. Brushett, *J. Electrochem. Soc.*, 2020, **167**, 124521.
123 P. Jeanty, C. Scherer, E. Magori, K. Wiesner-Fleischer, O. Hinrichsen and M. Fleischer, *J. CO_2 Util.*, 2018, **24**, 454–462.
124 B. De Mot, J. Hereijgers, M. Duarte and T. Breugelmans, *Chem. Eng. J.*, 2019, **378**, 122224.
125 F. Bidault, D. J. L. Brett, P. H. Middleton and N. P. Brandon, *J. Power Sources*, 2009, **187**, 39–48.
126 N. A. Hampson and A. J. S. McNeil, in *Electrochemistry*, ed. D. Pletcher, Royal Society of Chemistry, London, 1984, pp. 1–65.
127 A. Reyes, R. P. Jansonius, B. A. W. Mowbray, Y. Cao, D. G. Wheeler, J. Chau, D. J. Dvorak and C. P. Berlinguette, *ACS Energy Lett.*, 2020, **5**, 1612–1618.
128 U. O. Nwabara, A. D. Hernandez, D. A. Henckel, X. Chen, E. R. Cofell, M. P. De-Heer, S. Verma, A. A. Gewirth and P. J. A. Kenis, *ACS Appl. Energy Mater.*, 2021, **4**, 5175–5186.
129 M. E. Leonard, L. E. Clarke, P. D. A. Forner-Cuenca, D. S. M. Brown and P. D. F. R. Brushett, *ChemSusChem*, 2020, **13**, 400–411.
130 Y. Gao, X. Tu, X. Liu, Y. Zhang, M. Huang, J. Zhu and H. Jiang, *ChemCatChem*, 2024, **16**, e202400361.
131 M. Duarte, B. De Mot, D. J. Hereijgers and P. D. T. Breugelmans, *ChemElectroChem*, 2019, **6**, 5596–5602.
132 J. Lin, S. Yan, C. Zhang, Q. Hu and Z. Cheng, *Processes*, 2022, **10**, 826.

133 I. Moussallem, S. Pinnow, N. Wagner and T. Turek, *Chem. Eng. Process. Process Intensif.*, 2012, **52**, 125–131.

134 D. Franzen, B. Ellendorff, M. C. Paulisch, A. Hilger, M. Osenberg, I. Manke and T. Turek, *J. Appl. Electrochem.*, 2019, **49**, 705–713.

135 M. Li, M. N. Idros, Y. Wu, T. Burdyny, S. Garg, X. S. Zhao, G. Wanga and T. E. Rufford, *J. Mater. Chem. A*, 2021, **9**, 19369–19409.

136 M. Weissmann, S. Baranton, J. M. Clacens and C. Coutanceau, *Carbon*, 2010, **48**, 2755–2764.

137 L. W. McKeen, in *The Effect of Creep and Other Time Related Factors on Plastics and Elastomers*, ed. L. W. McKeen, William Andrew, New York, 2nd edn, 2009, pp. 337–372.

138 A. Z. Weber, *J. Power Sources*, 2010, **195**, 5292–5304.

139 F. Bienen, M. C. Paulisch, T. Mager, J. Osiewacz, M. Nazari, M. Osenberg, B. Ellendorff, T. Turek, U. Nieken, I. Manke and K. A. Friedrich, *Electrochem. Sci. Adv.*, 2023, **3**, e2100158.

140 L. M. Baumgartner, C. I. Koopman, A. Forner-Cuenca and D. A. Vermaas, *ACS Sustain. Chem. Eng.*, 2022, **10**, 4683–4693.

141 W. Ge, Y. Chen, Y. Fan, Y. Zhu, H. Liu, L. Song, Z. Liu, C. Lian, H. Jiang and C. Li, *J. Am. Chem. Soc.*, 2022, **144**, 6613–6622.

142 C. Zhu, G. Wu, J. Mao, A. Chen, Y. Zhao, G. Feng, Y. Wei, X. Liu, S. Li, G. Li, X. Dong, Y. Song, W. Wei and W. Chen, *Chem. Eng. J.*, 2024, **485**, 150040.

143 E. J. Dufek, T. E. Lister and M. E. McIlwain, *Electrochem. Solid-State Lett.*, 2012, **15**, B48.

144 S. S. Bhargava, F. Proietto, D. Azmoodeh, E. R. Cofell, D. A. Henckel, S. Verma, C. J. Brooks, A. A. Gewirth and P. J. A. Kenis, *ChemElectroChem*, 2020, **7**, 2001–2011.

145 V. R. Stamenkovic, D. Strmcnik, P. P. Lopes and N. M. Markovic, *Nat. Mater.*, 2017, **16**, 57–69.

146 L. Dunsmore, A. Uddin, H. Zhang, G. Wu and S. Litster, *J. Power Sources*, 2021, **506**, 230188.

147 Y. Zhao, L. Hao, A. Ozden, S. Liu, R. K. Miao, P. Ou, T. Alkayyali, S. Zhang, J. Ning, Y. Liang, Y. Xu, M. Fan, Y. Chen, J. E. Huang, K. Xie, J. Zhang, C. P. O'Brien, F. Li, E. H. Sargent and D. Sinton, *Nat. Synth.*, 2023, **2**, 403–412.

148 Z. Lu, W. Xu, J. Ma, Y. Li, X. Sun and L. Jiang, *Adv. Mater.*, 2016, **28**, 7155–7161.

149 Z. Cai, Y. Zhang, Y. Zhao, Y. Wu, W. Xu, X. Wen, Y. Zhong, Y. Zhang, W. Liu, H. Wang, Y. Kuang and X. Sun, *Nano Res.*, 2019, **12**, 345–349.

150 X. Dong, S. Li, C. Zhu, J. Mao, G. Wu, G. Li, G. Feng, A. Chen, Y. Wei, X. Liu, J. Wang, Y. Song, W. Chen and W. Wei, *Appl. Catal., B*, 2023, **336**, 122929.

151 P. Ding, H. Zhao, T. Li, Y. Luo, G. Fan, G. Chen, S. Gao, X. Shi, S. Lu and X. Sun, *J. Mater. Chem. A*, 2020, **8**, 21947–21960.

152 C. Zhu, G. Shen, W. Chen, X. Dong, G. Li, Y. Song, W. Wei and Y. Sun, *J. Power Sources*, 2021, **495**, 229814.

153 S. Li, W. Chen, X. Dong, C. Zhu, A. Chen, Y. Song, G. Li, W. Wei and Y. Sun, *Nat. Commun.*, 2022, **13**, 3080.

154 H. Rabiee, L. Ge, X. Zhang, S. Hu, M. Li and Z. Yuan, *Energy Environ. Sci.*, 2021, **14**, 1959–2008.

155 N. Weber, M. Möntmann, M. Wessling and R. Keller, *Chem. Eng. J.*, 2024, **486**, 150031.

156 R. Kas, K. K. Hummadi, R. Kortlever, P. De Wit, A. Milbrat, M. W. J. Luiten-Olieman, N. E. Benes, M. T. M. Koper and G. Mul, *Nat. Commun.*, 2016, **7**, 10748.

157 G. Chen, H. Rabiee, M. Li, B. Ma, Y. Kuang, F. Dorosti, Z. Zhu, H. Wang and L. Ge, *Adv. Mater.*, 2025, **37**, 2420391.

158 Y. Kuang, G. Chen, H. Rabiee, B. Ma, F. Dorosti, A. K. Nanjundan, Z. Zhu, H. Wang and L. Ge, *Energy Fuels*, 2024, **38**, 10096–10105.

159 A. Mustafa, B. G. Lougou, Y. Shuai, Z. Wang, H. U. Rehman, S. Razzaq, W. Wang, R. Pan and J. Zhao, *Front. Chem. Sci. Eng.*, 2024, **18**, 29.

160 X. Liu, S. Li, A. Chen, X. Dong, J. Mao, C. Zhu, G. Wu, Y. Wei, J. Xia, H. Zhu, X. Wang, Z. Xu, G. Li, Y. Song, W. Wei and W. Chen, *ACS Catal.*, 2025, **15**, 4259–4269.

161 N. Weber, J. Linkhorst, R. Keller and M. Wessling, *Adv. Mater. Technol.*, 2023, **8**, 2300720.

162 X. Wang, T. Liu, H. Li, C. Han, P. Su, N. Ta, S. P. Jiang, B. Kong, J. Liu and Z. Huang, *Nano Lett.*, 2023, **23**, 4699–4707.

163 W. Shao and X. Zhang, *Nanoscale*, 2021, **13**, 7081–7095.

164 M. B. Ross, Y. Li, P. De Luna, D. Kim, E. H. Sargent and P. Yang, *Joule*, 2019, **3**, 257–264.

165 B. Qin, Y. Li, H. Fu, H. Wang, S. Chen, Z. Liu and F. Peng, *ACS Appl. Mater. Interfaces*, 2018, **10**, 20530–20539.

166 J. Xiao, M. R. Gao, S. Liu and J. L. Luo, *ACS Appl. Mater. Interfaces*, 2020, **12**, 31431–31438.

167 M. Ma, E. L. Clark, K. T. Therkildsen, S. Dalsgaard, I. Chorkendorff and B. Seger, *Energy Environ. Sci.*, 2020, **13**, 977–985.

168 S. Ren, D. Joulié, D. Salvatore, K. Torbensen, M. Wang, M. Robert and C. P. Berlinguette, *Science*, 2019, **365**, 367–369.

169 N. S. R. Cuellar, K. Wiesner-Fleischer, M. Fleischer, A. Rucki and O. Hinrichsen, *Electrochim. Acta*, 2019, **307**, 164–175.

170 G. Chen, M. Hong, B. Ma, Y. Kuang, H. Rabiee, X. Xu, F. Dorosti, P. Yan, N. Shah, A. K. Nanjundan, Z. Zhu, H. Wang and L. Ge, *Appl. Catal. B Environ. Energy*, 2025, **381**, 125902.

171 K. Ye, A. Cao, J. Shao, G. Wang, R. Si, N. Ta, J. Xiao and G. Wang, *Sci. Bull.*, 2020, **65**, 711–719.

172 B. Ma, H. Rabiee, G. Chen, Y. Kuang, T. Zhu, P. Yan, L. Ge and Z. Zhu, *Chem. Eng. J.*, 2025, **523**, 168323.

173 Z. Zhao, J. Zhang, M. Lei and Y. Lum, *Nano Res. Energy*, 2023, **2**, e9120044.

174 Y. Wei, X. Wang, J. Mao, Y. Song, H. Zhu, X. Liu, C. Luo, S. Li, A. Chen, G. Li, X. Dong, W. Wei and W. Chen, *Angew. Chem.*, 2025, **137**, e202423370.

175 X. Wang, Y. Wei, Y. Song, J. Mao, X. Liu, S. Li, G. Li, H. Zhu, J. Xia, C. Luo, A. Chen, X. Dong, W. Wei and W. Chen, *Adv. Sci.*, 2025, **12**, e02947.

176 Z. Zhang, Y. Xia, K. Xu, F. Wang and S. Min, *ACS Appl. Energy Mater.*, 2024, **8**, 276–285.

177 C. Lu, P. Shi, S. Huang, C. Yang, J. Zhu, J. Zhang, C. Ke, Y. Su, X. Zhuang and T. Wang, *Angew. Chem., Int. Ed.*, 2025, **64**, e202423263.